



Search for supersymmetry in final states with a single electron or muon using angular correlations and heavy-object identification in proton-proton collisions at $\sqrt{s} = 13$ TeV

The CMS Collaboration

Abstract

A search for supersymmetry is presented in events with a single charged lepton, electron or muon, and multiple hadronic jets. The data correspond to an integrated luminosity of 138 fb^{-1} of proton-proton collisions at a center-of-mass energy of 13 TeV, recorded by the CMS experiment at the CERN LHC. The search targets gluino pair production, where the gluinos decay into final states with the lightest supersymmetric particle (LSP) and either a top quark-antiquark ($t\bar{t}$) pair, or a light-flavor quark-antiquark ($q\bar{q}$) pair and a virtual or on-shell W boson. The main backgrounds, $t\bar{t}$ pair and W +jets production, are suppressed by requirements on the azimuthal angle between the momenta of the lepton and of its reconstructed parent W boson candidate, and by top quark and W boson identification based on a machine-learning technique. The number of observed events is consistent with the expectations from standard model processes. Limits are evaluated on supersymmetric particle masses in the context of two simplified models of gluino pair production. Exclusions for gluino masses reach up to 2130 (2280) GeV at 95% confidence level for a model with gluino decay to a $t\bar{t}$ pair (a $q\bar{q}$ pair and a W boson) and the LSP. For the same models, limits on the mass of the LSP reach up to 1270 (1220) GeV.

Submitted to the Journal of High Energy Physics

1 Introduction

Supersymmetry (SUSY) [1–6] is an appealing extension of the standard model (SM) of particle physics, which is able to address several shortcomings of the SM by introducing a new symmetry that predicts superpartners to the existing bosons and fermions. The supersymmetric partner of the gluon is the gluino (\tilde{g}). The superpartners of the electroweak gauge bosons and the Higgs bosons mix to form mass eigenstates called neutralinos ($\tilde{\chi}^0$) and charginos ($\tilde{\chi}^\pm$). In SUSY models that conserve R -parity [7], the SUSY particles have to be produced in pairs and the lightest SUSY particle (LSP) is stable, providing a possible dark matter candidate.

The search in this paper targets final states containing a single lepton (electron or muon), missing transverse momentum, and large hadronic activity. The proton-proton (pp) collision data at $\sqrt{s} = 13$ TeV recorded by the CMS experiment at the CERN LHC during 2016–2018 and corresponding to an integrated luminosity of 138 fb^{-1} are used. By defining exclusive search regions (SRs) with and without b tagging requirements, the search is sensitive to different SUSY models. The sensitivity is further enhanced by using a large number of SR bins defined by several variables characterizing the event topology and kinematical properties. The results are interpreted in terms of simplified SUSY models [8–12].

The diagrams of the specific R -parity conserving models of gluino pair production that are used to interpret the results are shown in Fig. 1. The results of the search with at least one b -tagged jet, referred to as “multi- b analysis”, are interpreted in terms of the simplified model, labeled as “T1tttt” (left), where the gluino always decays to a top quark-antiquark pair ($t\bar{t}$) and the lightest neutralino ($\tilde{\chi}_1^0$), which is the LSP. The top quarks will decay into a bottom quark (b quark) and a W boson, which further decays hadronically or into a lepton and a neutrino. The observations in the SR bins with no b -tagged jets, referred to as “zero- b analysis”, are interpreted in the model labeled as “T5qqqqWW” (right). In this model, each gluino decays to a light-flavor quark-antiquark pair of different quark flavors ($q\bar{q}'$) and the lightest chargino ($\tilde{\chi}_1^\pm$), which then decays further to a $\tilde{\chi}_1^0$ and a W boson, which finally decays hadronically or into a lepton and a neutrino. In T5qqqqWW, the W boson can be virtual, depending on the mass difference between the lightest chargino ($\tilde{\chi}_1^\pm$) and the lightest neutralino ($\tilde{\chi}_1^0$). The mass of the $\tilde{\chi}_1^\pm$ is fixed at the value halfway between the masses of the \tilde{g} and the $\tilde{\chi}_1^0$.

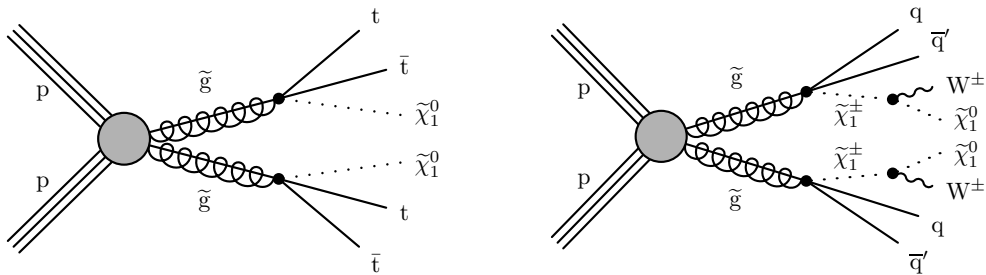


Figure 1: Diagrams showing the simplified SUSY models T1tttt (left) and T5qqqqWW (right).

Searches targeting gluino pair production in the single-lepton final state have been performed by both the ATLAS [13–17] and CMS [18–23] Collaborations. The investigated models have also been tested by ATLAS [24–27] and CMS [28–35] in other final states. The results presented in this paper supersede the CMS search presented in Ref. [19], which follows a similar strategy and uses data recorded in 2016, corresponding to an integrated luminosity of 35.9 fb^{-1} . Improvements stem not only from the larger analyzed data set, but also from significantly reduced SM background contributions in the SR. This is achieved by requiring at least one jet to

be consistent with a hadronically decaying top quark (W boson) in the multi- b (zero- b) final states as determined by multivariate classifiers.

Tabulated results are provided in the HEPData record for this analysis [36].

2 The CMS detector

The CMS apparatus is a multipurpose, nearly hermetic detector, designed to trigger on and identify electrons, muons, photons, and charged and neutral hadrons [37–39]. The detector comprises an all-silicon inner tracker and by the crystal electromagnetic calorimeter (ECAL) and brass-scintillator hadron calorimeters (HCAL), operating inside a 3.8 T superconducting solenoid, with data from the gas-ionization muon detectors embedded in the flux-return yoke outside the solenoid. Each of these parts of the detector is composed of a cylindrical barrel section and two endcap sections. The pseudorapidity (η) coverage of the barrel and endcap detectors is extended by forward calorimeters that lie very close to the LHC beam line. Outside the solenoid, the returning magnetic flux is guided through a steel return yoke. Gas-ionization detectors are sandwiched in between the layers of the return yoke and are used to detect muons.

The events used in the search were collected using a two-tiered trigger system. The first level, composed of custom hardware processors, uses information from the calorimeters and muon detectors to select events at a rate of around 100 kHz within a fixed latency of about $4 \mu\text{s}$ [40]. The second level, known as the high-level trigger (HLT), consists of a farm of processors running a version of the full event reconstruction software optimized for fast processing, and reduces the event rate to around 1 kHz before data storage [41]. The CMS detector is described in more detail, along with the coordinate system and basic kinematic variables, in Ref. [42].

3 Simulation

Simulated background events are used to optimize the event selection and test the background estimation, which is mainly based on control samples in data. The SM processes are simulated with different Monte Carlo (MC) event generators: Events for $t\bar{t}$, W +jets, and Drell–Yan (DY) production, as well as for the background from SM events composed uniquely of jets produced through the strong interaction, referred to as quantum chromodynamics (QCD) multi-jet events, are simulated using the MADGRAPH5_aMC@NLO event generator at leading order (LO) (versions 2.2.2 for 2016 and 2.4.2 for 2017 and 2018) [43]. The $t\bar{t}$ events are generated with up to three additional partons in the matrix-element calculations, while the W +jets and DY events are generated with up to four additional partons. Single top quark events produced through the s channel; events containing a $t\bar{t}$ pair produced in association with a Z boson, a W boson, or a photon; and rare events such as those containing multiple electroweak or Higgs bosons (W , Z , γ , and H) are generated with MADGRAPH5_aMC@NLO at next-to-LO (NLO) [44]. Events containing a single top quark produced through the t channel and tW production, as well as WW and $t\bar{t}H$ events, are calculated at NLO with the POWHEG v1 (v2) [45–52] program for 2016 (2017 and 2018). The ZZ events are generated at NLO with either POWHEG or MADGRAPH5_aMC@NLO, depending on the decay mode, while WZ production is simulated at LO with PYTHIA 8.226 (8.230) [53] for 2016 (2017 and 2018). The normalization of the simulated background samples is performed using the most accurate cross section calculations available [43, 48, 49, 54–65], which typically correspond to NLO or next-to-NLO (NNLO) accuracy.

Simulated signal events are used to optimize the event selection and to estimate the signal

acceptance and selection efficiency. They are generated using `MADGRAPH5_aMC@NLO` at LO including up to two additional partons in the matrix-element calculations. The production cross sections are determined with approximate NNLO plus next-to-next-to-leading logarithmic (NNLL) corrections [66–76]. The signal events are produced on a two-dimensional grid for different gluino and LSP masses.

The parton showering and hadronization for all simulated samples is performed with the `PYTHIA 8.226 (8.230)` program for 2016 (2017 and 2018). For samples that are simulated at NLO with `MADGRAPH5_aMC@NLO`, the partons from the matrix-element calculations are matched to those from the parton showers using the `FxFx` [44] scheme, while for samples simulated at LO the `MLM` scheme [77] is adopted. The `CUETP8M1` [78] `PYTHIA 8.226` tune is used for both SM and signal samples for the analysis of the 2016 data. For 2017 and 2018, the `CP5 (CP2)` [79] tunes are used for the SM background (signal) samples. Simulated background samples generated at LO (NLO) with the `CUETP8M1` tune use the `NNPDF3.0LO (NNPDF3.0NLO)` [80] sets for the parton distribution functions (PDFs), respectively. For signal samples, the `NNPDF3.1LO` was used [81]. The samples using the `CP2` or `CP5` tune use the `NNPDF3.1LO` or `NNPDF3.1NNLO` sets, respectively.

Simulated SM events are processed through a `GEANT4`-based [82] simulation of the CMS detector, while the simulated signal events are processed through the CMS fast simulation program [83, 84] in order to save computing time. The results of the fast simulation are found to be generally consistent with the `GEANT4`-based simulation.

All simulated events are generated with nominal distributions of additional `pp` interactions per bunch crossing and nearby bunch crossings, referred to as pileup. Any residual difference between the pileup distribution used in the simulation and the one observed in the data is corrected via a weighting procedure applied to the simulated events.

In order to improve the modeling of additional jets originating mainly from initial-state radiation (ISR) in events containing `t \bar{t}` , the `MADGRAPH5_aMC@NLO` prediction is compared to data in a `t \bar{t}` -enriched dileptonic control region, and scale factors (SF) are extracted that are applied to the 2016–2018 `t \bar{t}` simulation as well as to the SUSY signal simulation. The `t \bar{t}` simulation of the years 2017 and 2018 is performed with an updated tune resulting in a good agreement between simulation and data, such that no SF are needed.

4 Object reconstruction

The “particle-flow” (PF) algorithm [85] aims to reconstruct and identify each particle in an event, with an optimized combination of information from the various elements of the CMS detector, and classifies each either as a photon, electron, muon, charged hadron, or a neutral hadron. The energy of charged hadrons is determined from a combination of their momentum measured in the tracker and the matching ECAL and HCAL energy deposits, corrected for the response function of the calorimeters to hadronic showers. The energy of neutral hadrons is obtained from the corresponding corrected ECAL and HCAL energies. The primary vertex (PV) is taken to be the vertex corresponding to the hardest scattering in the event, evaluated using tracking information alone, as described in Section 9.4.1 of Ref. [86].

The energy and momentum of electrons is determined from a combination of the electron momentum at the PV as determined by the tracker, the energy of the corresponding ECAL cluster, and the energy sum of all bremsstrahlung photons spatially compatible with originating from the electron track [37]. For electrons with transverse momentum $p_T \approx 45$ GeV from $Z \rightarrow e^+e^-$

decays, the momentum resolution ranges from 1.7 to 4.5%. It is generally better in the barrel region than in the endcaps, and also depends on the bremsstrahlung energy emitted by the electron as it traverses the material in front of the ECAL.

The energy of muons is obtained from the curvature of the corresponding track. Muons are measured in the range $|\eta| < 2.4$, with detection planes made using three technologies: drift tubes, cathode strip chambers, and resistive plate chambers. Matching muons to tracks measured in the tracker results in a relative p_T resolution of 1% in the barrel and 3% in the endcaps for muons with p_T up to 100 GeV, and of better than 7% in the barrel for muons with p_T up to 1 TeV [38].

A relative isolation variable is defined as the p_T sum of all objects within a cone around the lepton candidate (excluding the candidate itself), divided by the lepton p_T . This analysis uses the so-called mini-isolation variable (I_{mini}), which is an optimized version [21] of the originally proposed mini-isolation in Ref. [87]. The cone size R , referring to the distance in the ϕ - η plane (where ϕ is the azimuthal angle), depends on the p_T of the lepton: for $p_T < 50$ GeV, $R = 0.2$; for $50 < p_T < 200$ GeV, $R = 10 \text{ GeV} / p_T$; and for $p_T > 200$ GeV, $R = 0.05$.

Two categories of leptons are defined, denoted by “veto leptons” and “good leptons”, in the range of $|\eta| < 2.4$ and with a minimum p_T threshold of 10 and 25 GeV, respectively. Muons that fulfill the “loose” working point (WP) of the standard muon identification (ID) criteria [38] are defined as “veto muons”. The dedicated “veto” WP of the standard electron ID criteria [37] is used to define “veto electrons”. We use a common requirement of $I_{\text{mini}} < 0.4$ for all veto leptons, whereas for good muons (electrons) $I_{\text{mini}} < 0.2$ (0.1) is required. The use of I_{mini} enhances the selection efficiency of signal events that contain a large amount of hadronic energy compared to an isolation definition with a fixed cone size. The efficiency for reconstructing a veto muon exceeds 99% and is equal to 95% for a veto electron. The “medium” WP of the muon ID criteria with an efficiency of more than 98% is used to select good muons. Good electrons are selected using the “tight” WP of the electron ID criteria with an efficiency of 70%. A conversion veto and the requirement of zero lost hits in the tracker are applied for good electrons to reject converted photons.

Jets are clustered with the anti- k_T algorithm [88, 89] with a distance parameter R of 0.4 (AK4), or, in order to identify large-radius jets, with $R = 0.8$ (AK8). The jet p_T is determined from the vectorial \vec{p}_T sum of all particles in the jet, and is found from simulation to be, on average, within 5 to 10% of the true p_T over the whole p_T spectrum and detector acceptance. Pileup interactions contribute additional tracks and calorimetric energy depositions, increasing the apparent jet momentum. To mitigate this effect, different strategies are applied. For AK4 jets, tracks identified to be originating from pileup vertices are discarded and a correction for remaining contributions is applied [90]. For AK8 jets, the pileup per particle identification algorithm [90, 91] is used, which makes use of local shape information, event pileup properties, and tracking information. A local shape variable is defined, which distinguishes between collinear and soft diffuse distributions of other particles surrounding the particle under consideration. The former is attributed to particles originating from the hard scatter and the latter to particles originating from pileup interactions. Charged particles identified to be originating from pileup vertices are discarded. For each neutral particle, a local shape variable is computed using the surrounding charged particles compatible with the primary vertex within the tracker acceptance ($|\eta| < 2.5$), and using both charged and neutral particles in the region outside of the tracker coverage. The momenta of the neutral particles are then rescaled according to their probability to originate from the primary interaction vertex deduced from the local shape variable, superseding the need for jet-based pileup corrections [90]. In the following, “jet” will refer

to AK4 jets, unless specified otherwise.

We apply jet energy corrections, derived from simulation studies, to match the average measured energy of jets to that of particle-level jets. In situ measurements of the momentum balance in dijet, photon+jet, Z+jet, and multijet events are used to determine any residual differences between the jet energy scale in data and in simulation, and appropriate corrections are applied in the analysis [92]. For the fast simulation that is used for the signal, dedicated jet energy corrections are applied.

Additional selection criteria are applied to each jet to remove jets potentially affected by instrumental effects or reconstruction failures [90]. The jets are selected with $p_T > 30$ GeV and $|\eta| < 2.4$. The jets that lie within a cone of $R = 0.4$ around any good or veto lepton are removed, to avoid double counting.

To identify jets originating from b quarks we use an inclusive deep neural network based combined secondary vertex tagger is used at the medium WP [93]. The efficiency to identify b jets varies between 50 and 70%, depending on the jet p_T , with a misidentification probability of 10–15% for c jets and 1–5% for light-flavor quark and gluon jets, also depending on the jet p_T .

AK8 jets are selected with $p_T > 200$ GeV and $|\eta| < 2.4$. In order to identify hadronic decays of top quarks and W bosons with a large Lorentz boost, we apply a dedicated algorithm that is based on convolutional neural networks, the DeepAK8 algorithm [94]. It is a multiclass classifier for top quark, W boson, Z boson, Higgs boson, and QCD jets, and takes input from all the PF candidates and secondary vertices associated with the AK8 jet.

Hadronically decaying top quarks with $p_T > 400$ GeV are usually merged into one large-radius jet, and are identified using the DeepAK8 algorithm at an efficiency of $\approx 68\%$ and a mistagging rate of $\approx 8\%$, as computed in a W+jets sample. The dominant source of the mistagging rate stems from QCD multijet events. Top quarks with $p_T < 400$ GeV are usually not boosted enough to be caught in one large-radius jet cone, and therefore are identified by a resolved top quark tagging (t tagging) algorithm, as used in Ref. [95]. It identifies hadronically decaying top quarks whose decay products form three individual jets. A boosted decision tree is used to distinguish between trijet combinations whose three jets all match the decay products of a top quark versus those that do not. It uses high-level information such as the invariant mass of the trijet as well as information from each jet. The resolved t tagger yields an efficiency of $\approx 42\%$, while the mistagging rate is $\approx 4\%$.

To avoid double counting, a cross cleaning between resolved and merged t tags is performed by first reconstructing the merged top quarks as identified by the DeepAK8 algorithm. In the next step, resolved top quark candidates that contain any jet within a cone of radius $R = 0.8$ of the merged top quark (i.e., the cone of the AK8 jet classified as a top quark by the DeepAK8) are removed. In the following, n_t is used to denote the number of identified t tags.

Hadronically decaying W bosons are identified with the DeepAK8 algorithm as well. For the zero-b analysis, this tagging algorithm utilizes AK8 jets to identify hadronically decaying W bosons with $p_T > 200$ GeV. The efficiency for W boson tagging is $\approx 62\%$, while the mistagging rate is $\approx 7\%$. The number of identified W bosons is denoted as n_W .

All mistagging rates for the heavy object taggers were measured in W+jets data samples, where the W decays leptonically. The efficiencies of these taggers were measured using MC simulation samples of hadronic t and W decays.

The missing transverse momentum vector \vec{p}_T^{miss} is computed as the negative vector p_T sum of all the PF candidates in an event, and its magnitude is denoted as p_T^{miss} [96]. The \vec{p}_T^{miss} is

modified to account for corrections to the energy scale of the reconstructed jets in the event. Anomalous high- p_T^{miss} events can occur because of a variety of reconstruction failures, detector malfunctions, or noncollision backgrounds. Such events are rejected by event filters that are designed to identify more than 85–90% of the spurious high- p_T^{miss} events with an error rate of less than 0.1%.

Two kinematic variables are used to describe the energy scale of an event: The L_T variable is defined as the scalar sum of the lepton p_T and p_T^{miss} , reflecting the “leptonic” energy scale of the event. The H_T variable reflects the “hadronic” energy scale of the event. It denotes the scalar p_T sum of all selected jets.

In the second half of the 2018 data-taking period, a detector malfunction prevented the readout from a small fraction of the HCAL. This is taken into account by reweighting simulated events such that it reflects the overall 2018 efficiency of the HCAL in the relevant region.

5 Baseline event selection

Events are selected with a combination of HLT paths, relying on the kinematic variables of reconstructed leptons, H_T , p_T^{miss} , or combinations thereof, to maximize the trigger efficiency. The main HLT path requires a loosely isolated lepton with $p_T > 15$ GeV and H_T greater than a threshold equal to 350, 400, and 450 GeV for 2016, 2017, and 2018, respectively. The additional HLT paths require p_T^{miss} greater than a threshold equal to 100, 110, and 120 GeV for the three data-taking years; isolated electrons with $p_T > 27$ (35) GeV in 2016 (2017 and 2018); isolated muons with $p_T > 24$ GeV; or leptons with no isolation requirement and a higher p_T threshold of 105 or 115 GeV for electrons (depending on the year), or 50 GeV for muons. The trigger efficiency is measured in control samples recorded either with single-lepton triggers or with triggers based on an H_T requirement. For the electron channel, it is found to be 98, 93, and 97% in 2016, 2017, and 2018, respectively, while for the muon channel it is 99% for all three data-taking years. The inefficiency is mainly caused by the lepton selection in the trigger. The uncertainty in the measured trigger efficiencies is about 1%.

For the baseline event selection, one good lepton with $p_T > 25$ GeV is required, and events with additional veto leptons with $p_T > 10$ GeV are removed. Events with two genuine leptons, of which one is not identified, constitute one of the main backgrounds in the SR bins. In order to reduce this background contribution, we remove events with an isolated track that could stem from leptons that are not well identified, but are not removed by the requirement of no veto leptons. Charged particle tracks from the PV with $p_T > 5$ GeV are selected, and an isolation variable I_{rel} is defined as the p_T sum of all tracks within a cone of $R = 0.3$ around the track candidate (excluding the candidate itself), divided by the track p_T . The isolated tracks considered here come from two different sources, one is from isolated leptons that satisfy looser ID criteria than lepton candidates, and the other from isolated charged hadrons. Charged hadron (lepton) candidates are required to satisfy $I_{\text{rel}} < 0.1$ (0.2). In case of multiple isolated track candidates in an event, the one with the highest p_T that has the opposite charge with respect to the selected lepton is chosen. Events with such isolated tracks are rejected if the m_{T2} variable [97], calculated from the momenta of the isolated track and the selected lepton, is below 60 (80) GeV for isolated tracks associated with charged hadrons (leptons).

Furthermore, we require $H_T > 500$ GeV and $L_T > 250$ GeV. The usage of L_T instead of p_T^{miss} allows the analysis to be not only sensitive to events with high p_T^{miss} , but also to signal events with very low p_T^{miss} but higher lepton p_T . A minimum number of three jets is required for the baseline selection, and the two highest p_T jets are required to fulfill $p_T > 80$ GeV.

Events are selected exclusively for the multi-b or the zero-b analysis, depending on the number of b-tagged jets in the event. Events in the multi-b analysis are additionally required to contain at least one t tag. The baseline event selection is summarized in Table 1.

Table 1: Baseline event selection.

One good lepton with $p_T > 25$ GeV
No additional veto lepton with $p_T > 10$ GeV
No isolated track with $p_T > 5$ GeV with $m_{T2} < 60$ (80) GeV for hadronic (leptonic) tracks
$L_T > 250$ GeV
$H_T > 500$ GeV
Number of AK4 jets $n_{\text{jet}} \geq 3$
At least 2 jets with $p_T > 80$ GeV
$n_b \geq 1$ and $n_t \geq 1$ (multi-b analysis) or $n_b = 0$ (zero-b analysis)

6 Search strategy and background estimation

The central kinematic variable of this analysis is the absolute value of the azimuthal angle $\Delta\phi$ between the \vec{p}_T of a hypothetical W boson decaying leptonically and that of the decay lepton

$$\Delta\phi = \angle(\vec{p}_T^\ell, \vec{p}_T^W), \quad (1)$$

where the \vec{p}_T of the W boson candidate is reconstructed as $\vec{p}_T^W = \vec{p}_T^\ell + \vec{p}_T^{\text{miss}}$. After the baseline event selection, the main backgrounds are events containing one lepton and jets from $t\bar{t}$ or W+jets decays. These backgrounds contain both one prompt lepton and one neutrino from the W boson decay in the final state. Since the neutrino and lepton are boosted in the direction of the momentum of the W boson and the neutrino is the only source of \vec{p}_T^{miss} , a small $\Delta\phi$ value is expected. On the other hand, the SUSY models with two neutralinos in the final state break this correlation, because the neutralinos cannot be detected in the CMS detector and both of them will contribute to the \vec{p}_T^{miss} , randomizing its direction. This behavior is indeed observed in Fig. 2 showing simulated $\Delta\phi$ distributions. While most background contributions are at low $\Delta\phi$ values, the signal is almost flat over the whole range.

The effect of the t tagging in the multi-b analysis is shown in Fig. 3 for the sum of all background contributions and for two representative signal models with a (gluino, neutralino) mass of (2.2, 0.1) TeV and (1.8, 1.3) TeV. While the background in the SR at high $\Delta\phi$ is reduced by an order of magnitude when requiring one t tag, the signal yield is only slightly decreased. Therefore, one t tag is always required, and a few SR bins are defined to have two or more. When applying W boson tagging at the “tight” WP in the zero-b analysis, the signal is reduced by about 40%, while the W+jets background is reduced by more than 90%. The SR bins are split to contain events with either $n_W = 0$ or $n_W \geq 1$.

The $\Delta\phi$ variable is used to further suppress the background contributions. The regions with large $\Delta\phi$ above a threshold value $\Delta\phi_0$ are defined as SRs, while those with small $\Delta\phi$ values are used as control regions (CRs). For the multi-b analysis, the SR is defined by $\Delta\phi > 0.75$, whereas in the zero-b analysis the $\Delta\phi$ threshold depends on L_T and ranges between 0.5 and 1. This accounts for a possible higher boost of the W boson and correspondingly smaller $\Delta\phi$ at larger values of L_T . The SR is split into bins of n_{jet} , n_b , L_T , and H_T , and further categorized by n_t (n_W) for the multi-b (zero-b) analysis. The different SRs must provide good sensitivity for the different signal models and signal parameters, while ensuring sufficient statistical accuracy in CRs to predict the background in the corresponding SR.

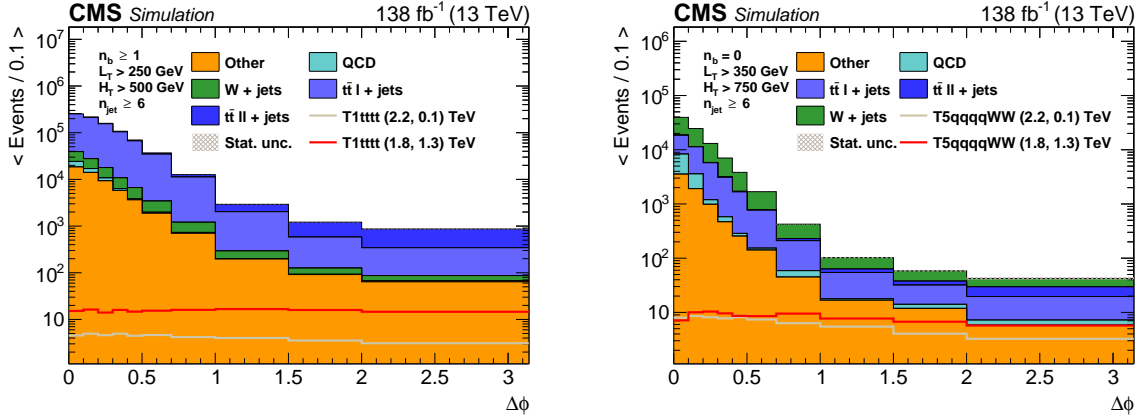


Figure 2: Signal and background distributions of the $\Delta\phi$ variable, as predicted by simulation, for the multi-b analysis, requiring $n_{\text{jet}} \geq 6$, $L_T > 250$ GeV, $H_T > 500$ GeV (left), and the zero-b analysis, requiring $n_{\text{jet}} \geq 6$, $L_T > 350$ GeV, $H_T > 750$ GeV (right). The predicted signal distributions are also shown for two representative combinations of (gluino, neutralino) masses with large (2.2, 0.1) TeV and small (1.8, 1.3) TeV mass differences.

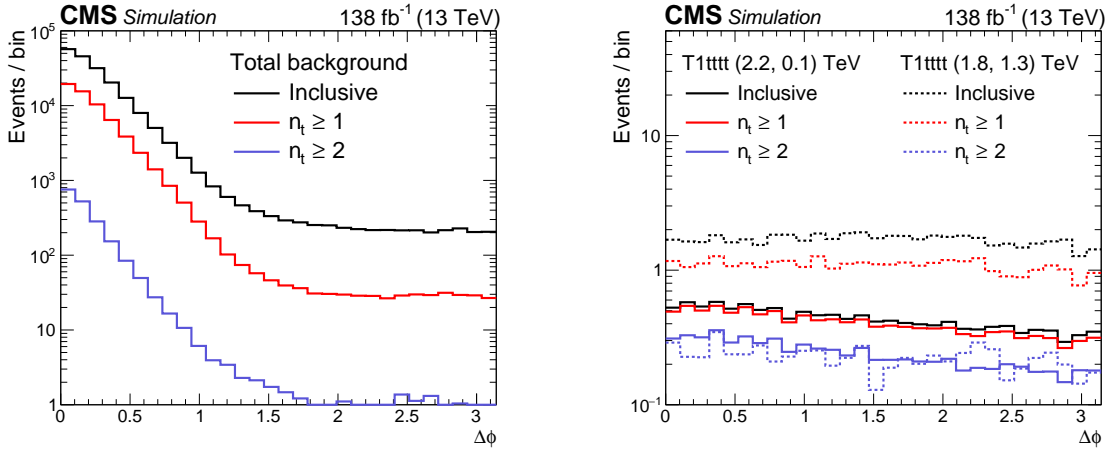


Figure 3: Distributions of $\Delta\phi$ as obtained from simulation, requiring various t tag multiplicities for the total background (left) and for the signal in two representative combinations of (gluino, neutralino) masses with large (2.2, 0.1) TeV and small (1.8, 1.3) TeV mass difference (right).

The principal tool to estimate the background contributions in the SR bins is a transfer factor, called R^{CS} , from CR to SR, which is measured in data with lower jet multiplicity, for each SR bin separately. For this estimation, we split the regions into a low- n_{jet} region, which is called the sideband (SB), and a high- n_{jet} region, which is called the mainband (MB). Both of these bands are further divided by $\Delta\phi$ into a CR (with $\Delta\phi < \Delta\phi_0$) and an SR (with $\Delta\phi > \Delta\phi_0$) as described above. This method can be considered as a factorization approach in $\Delta\phi$ and jet multiplicity with four regions indexed by pairs of CR or SR and SB or MB. We note that signal contamination in the SB SR, SB CR, and MB CR is small, typically $< 0.5\%$ for both multi-b and zero-b analysis, and is taken into account in the final fit.

To account for possible deviations from the factorization assumption in the extrapolation from SB to MB, we define multiplicative correction factors κ , determined from simulations, as described in Sections 6.1 and 6.2.

In the multi-b analysis, the background is dominated by $t\bar{t}$ events. In regions with one b-tagged

jet and four or five jets, about 80% $t\bar{t}$ events and 15 to 20% W +jets and single top quark events are expected, with small contributions from QCD multijet events. In all other multi-b regions, the $t\bar{t}$ background contribution is completely dominant. With only one SM process dominating the background contribution, a single R^{CS} factor is defined in the multi-b analysis for each SR bin, after having subtracted the small QCD multijets contribution in the SB. The background estimation is performed for each year and explained in detail in Section 6.1.

In the zero-b analysis, backgrounds from $t\bar{t}$ production are suppressed and contributions from W +jets production are found to be of the same size. Here, an extension of the multi-b strategy is employed, which takes into account differences in the R^{CS} values for these two backgrounds, for all years combined, as detailed in Section 6.2.

An overview of the (n_{jet}, n_b) regions used in this analysis is given in Fig. 4. The multi-b and the zero-b analysis share SB regions, but their MB SR bins are exclusive and are never used simultaneously, since the results are interpreted in different simplified models.

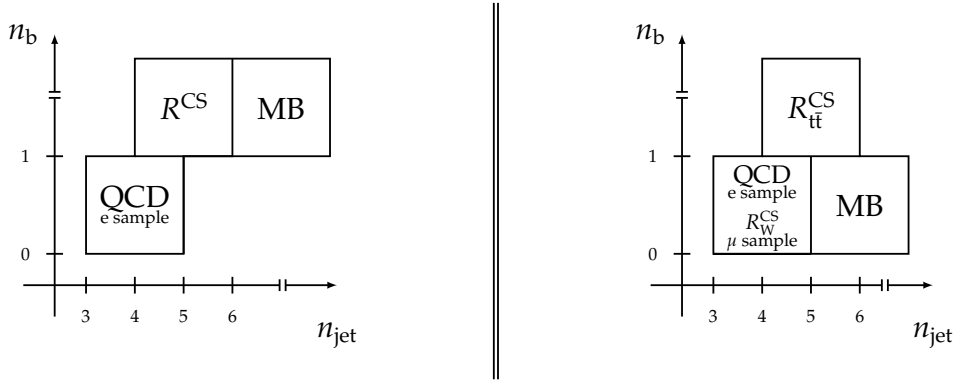


Figure 4: Overview of the regions used to calculate R^{CS} for the multi-b (left) and zero-b (right) analysis. For the multijet (QCD) fit, the electron (e) sample is used, while the muon (μ) sample is used for the determination of R^{CS}_{W} .

6.1 Background estimate in the multi-b final state

In the multi-b analysis, the predicted number $N_{\text{Pred}}^{\text{MB,SR}}$ of background events in each MB SR bin is given as the sum of the number of background events from $t\bar{t}$ and electroweak processes $N_{\text{Pred,EW}}^{\text{MB,SR}}$ and the number of QCD multijet events $N_{\text{Pred,QCD}}^{\text{MB,SR}}$:

$$N_{\text{Pred}}^{\text{MB,SR}} = N_{\text{Pred,EW}}^{\text{MB,SR}} + N_{\text{Pred,QCD}}^{\text{MB,SR}}. \quad (2)$$

The generic label “EW” refers to all backgrounds other than QCD multijet events. About 10–15% of the SM background events in the SB CR are expected to be QCD multijet events, while this fraction is significantly smaller in the MB SR. This background contribution is estimated independently from a fit to data, as described in Section 6.4. The multijet background is subtracted from the number of background events when calculating the transfer factor $R^{\text{CS}}_{\text{data}}$ from data:

$$R^{\text{CS}}_{\text{data}}(n_{\text{jet}} \in [4, 5]) = \frac{N_{\text{data}}^{\text{SB,SR}} - N_{\text{Pred,QCD}}^{\text{SB,SR}}}{N_{\text{data}}^{\text{SB,CR}} - N_{\text{Pred,QCD}}^{\text{SB,CR}}}. \quad (3)$$

Here, $N_{\text{data}}^{\text{SB,SR}}$ is the number of events in the SB SR, while $N_{\text{data}}^{\text{SB,CR}}$ corresponds to the number of events in the SB CR. The independently estimated number of multijet events for these two regions are $N_{\text{Pred,QCD}}^{\text{SB,SR}}$ and $N_{\text{Pred,QCD}}^{\text{SB,CR}}$.

The SB region, where R^{CS} is determined for each SR bin, is required to have four or five jets, while the MB region must satisfy $n_{\text{jet}} \in [6, 8]$ or $n_{\text{jet}} \geq 9$. This is represented graphically in Fig. 5 (left). The R^{CS} factor is calculated separately for each search bin in L_T , H_T , n_b , and n_t . At very high H_T , R^{CS} is determined jointly across all three n_b bins to increase the number of events, as the overall uncertainty of the background prediction for several of the search bins is dominated by the statistical uncertainty of the yield in the SB SR.

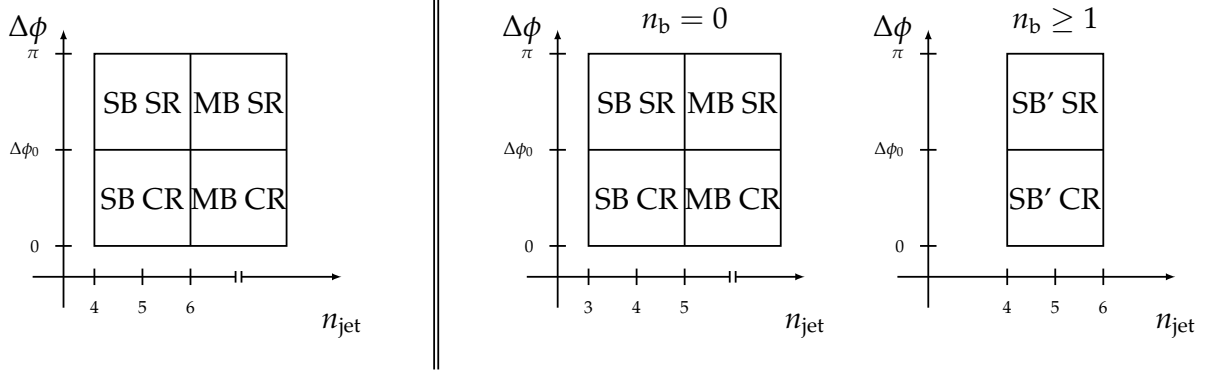


Figure 5: Graphical presentation of the regions indexed by pairs of SB or MB and CR or SR: for the multi-b (left) and for the zero-b (middle and right) analysis. The value of $\Delta\phi$ separating CR and SR is labeled as $\Delta\phi_0$. It is independent of the SR bin for the multi-b analysis with a value of 0.75, but varies from 0.5 to 1 among the zero-b SR bins.

Small differences in R^{CS} between SB and MB are corrected by the additional factor κ_{EW} , which is determined in simulation as the ratio of the R^{CS} for simulated events:

$$\kappa_{\text{EW}} = \frac{R_{\text{MC,EW}}^{\text{CS}}(n_{\text{jet}} \text{ as in MB})}{R_{\text{MC,EW}}^{\text{CS}}(n_{\text{jet}} \in [4, 5])}. \quad (4)$$

For the multi-b analysis, the label “ n_{jet} as in MB” refers to either $n_{\text{jet}} \in [6, 8]$ or $n_{\text{jet}} \geq 9$, depending on the specific search bin. The κ_{EW} factor is determined separately for each search bin, except that a common κ_{EW} factor is applied for the $n_b \geq 2$ search bins with the same H_T and L_T , since the κ_{EW} factors are found to be nearly independent of n_b . In general, these correction factors are found to be close to unity, within 20–30%. With these definitions, the number of predicted EW events in the MB SR is given by:

$$N_{\text{Pred,EW}}^{\text{MB,SR}} = \kappa_{\text{EW}} R_{\text{data}}^{\text{CS}}(n_{\text{jet}} \in [4, 5]) \left(N_{\text{data}}^{\text{MB,CR}} - N_{\text{Pred,QCD}}^{\text{MB,CR}} \right). \quad (5)$$

For events containing one lepton and jets from $t\bar{t}$ production, R^{CS} typically has values of 0.01 to 0.02, depending on the search bin. Similar values, ranging from 0.01 to 0.04, are found for W +jets events. In events with more than one high- p_T neutrino, e.g., in $t\bar{t}$ events in which both W bosons decay leptonically, R^{CS} is higher with values of around 0.5. This is expected, since a large fraction of background events at high $\Delta\phi$ is due to the dileptonic $t\bar{t}$ background, while the low- $\Delta\phi$ region is dominated by events with only one neutrino. A larger R^{CS} is also expected for events with three neutrinos, such as $t\bar{t}Z$, when the $t\bar{t}$ system decays into a lepton and jets and the Z boson decays to two neutrinos.

A small fraction of the background arises from dileptonic $t\bar{t}$ events in which one lepton is undetected. Having fewer jets than single-lepton $t\bar{t}$ events, these events tend to populate the SB. At the same time their $\Delta\phi$ distribution is flatter, leading to an overestimate of R^{CS} . Accordingly a separate correction is developed as described in Section 6.3.

6.2 Background estimate in the zero-b final state

Unlike the multi-b analysis, where we have only one dominant background in each bin, the SR bins in the zero-b analysis require the prediction of two backgrounds of almost the same size, $t\bar{t}$ and W +jets events. These background contributions are estimated by applying the R^{CS} method separately for each of the two components. Since we split these two contributions in the background estimation, we typically have smaller bin counts compared to the multi-b and consequently larger statistical fluctuations. To guarantee sufficient statistical precision, we perform the prediction for the full data set instead of separate estimations for 2016, 2017, and 2018.

This strategy implies the use of two sidebands enriched in W +jets (SB) and $t\bar{t}$ events (SB'), respectively. We decompose the total background in each bin, for example in the MB SR, as:

$$N_{\text{Pred}}^{\text{MB,SR}} = N_{\text{Pred,W}}^{\text{MB,SR}} + N_{\text{Pred,t}\bar{t}}^{\text{MB,SR}} + N_{\text{MC,other}}^{\text{MB,SR}} + N_{\text{Pred,QCD}}^{\text{MB,SR}}, \quad (6)$$

where the numbers of predicted W +jets and $t\bar{t}$ events are denoted by $N_{\text{Pred,W}}^{\text{MB,SR}}$ and $N_{\text{Pred,t}\bar{t}}^{\text{MB,SR}}$ respectively. We also include WW and WZ events, where the W boson decays leptonically and the second W or the Z boson hadronically, as a part of W +jets estimation, since they have similar kinematic properties and R^{CS} values. All other diboson events are treated as part of the rare backgrounds, which are estimated from simulation and denoted by $N_{\text{MC,other}}^{\text{MB,SR}}$. The small contribution of the QCD multijet background is fixed to the yield estimated from data as described in Section 6.4 and noted as $N_{\text{Pred,QCD}}^{\text{MB,SR}}$.

The $t\bar{t}$ and the W +jets contributions are estimated with an R^{CS} method in a similar way as described in the previous section. The R^{CS} values for W +jets and $t\bar{t}$ events are measured in separate SB regions with different b-tagged jet requirements, as laid out in Fig. 5 middle and right, respectively.

Similarly to Eq. (3), the value of R^{CS} for $t\bar{t}$ events is calculated in the multi-b sideband (SB') with $n_{\text{jet}} \in [4, 5]$ and $n_b \geq 1$. The differences are the definition of $\Delta\phi_0$ and the requirements that define the corresponding search bins:

$$R_{\text{data}}^{\text{CS}}(n_{\text{jet}} \in [4, 5], n_b \geq 1) = \frac{N_{\text{data}}^{\text{SB',SR}} - N_{\text{Pred,QCD}}^{\text{SB',SR}}}{N_{\text{data}}^{\text{SB',CR}} - N_{\text{Pred,QCD}}^{\text{SB',CR}}}. \quad (7)$$

A correction factor κ_b , defined in Eq. (8) and appearing in Eq. (11) below, accounts for the difference of $R_{\text{t}\bar{t}}^{\text{CS}}$ between samples with zero b-tagged jets and samples with at least one b-tagged jet and also takes into account non- $t\bar{t}$ background components in the EW category. It is taken from simulation:

$$\kappa_b = \frac{R_{\text{t}\bar{t}}^{\text{CS}}(n_{\text{jet}} \in [4, 5], n_b = 0)}{R_{\text{EW}}^{\text{CS}}(n_{\text{jet}} \in [4, 5], n_b \geq 1)}, \text{ where } R_{\text{MC}}^{\text{CS}} = \frac{N_{\text{MC}}^{\text{SB',SR}}}{N_{\text{MC}}^{\text{SB',CR}}} \text{ and } \text{MC} \in [t\bar{t}, \text{EW}]. \quad (8)$$

A second factor $\kappa_{\text{t}\bar{t}}$, defined in Eq. (9) and appearing in Eq. (11) below, corrects for a residual dependence of $R_{\text{t}\bar{t}}^{\text{CS}}$ on n_{jet} , in analogy to the κ_{EW} factor defined in Section 6.1. It is defined as:

$$\kappa_{\text{t}\bar{t}} = \frac{R_{\text{t}\bar{t}}^{\text{CS}}(n_{\text{jet}} \text{ as in MB}, n_b = 0)}{R_{\text{t}\bar{t}}^{\text{CS}}(n_{\text{jet}} \in [4, 5], n_b = 0)}. \quad (9)$$

Similar to the multi-b analysis, the number of simulated dilepton $t\bar{t}$ events in the factor $\kappa_{\text{t}\bar{t}}$ is corrected by the slight difference in the n_{jet} shape measured in dilepton and one-lepton CRs,

as described in Section 6.3. The product of both correction factors κ_b and $\kappa_{t\bar{t}}$ has typical values of 0.7 to 1.0 and statistical uncertainties from the simulation are propagated to the predicted yields.

Finally, the fraction of $t\bar{t}$ and W +jets events in the MB CR is estimated by a template fit to the n_b distribution for each search bin. The number of QCD events in these fits is consistently fixed to the number of events predicted from data as described in Section 6.4, while all other rare backgrounds are taken from simulation and fixed in the fit as well. The templates are taken from simulation. Only the number of $t\bar{t}$ and W +jets events is adjusted in the fit. The fractions are:

$$f_{\text{MC}}^{\text{MB,CR}} = \frac{N_{\text{fit,MC}}^{\text{MB,CR}}}{N_{\text{data}}^{\text{MB,CR}}}, \text{ with MC} \in [t\bar{t}, W+\text{jets}]. \quad (10)$$

The uncertainties in these two components are propagated as systematic uncertainties to the final prediction.

The final $t\bar{t}$ prediction is:

$$N_{\text{Pred},t\bar{t}}^{\text{MB,SR}} = \underbrace{\kappa_b \kappa_{t\bar{t}} R_{\text{data}}^{\text{CS}}(n_b \geq 1, n_{\text{jet}} \in [4, 5])}_{\text{transfer factor}} \underbrace{f_{t\bar{t}}^{\text{MB,CR}} N_{\text{data}}^{\text{MB,CR}}}_{t\bar{t} \text{ contribution in the control region}}. \quad (11)$$

The W +jets contribution $N_{\text{Pred},W}^{\text{MB,SR}}$ is also estimated using an R^{CS} method. The zero-b SB is chosen with $n_{\text{jet}} \in [3, 4]$, $n_b = 0$. With respect to the SB used for the estimate of $R_{t\bar{t}}^{\text{CS}}$, a lower jet multiplicity is chosen in order to limit the contamination from $t\bar{t}$ events. Here we select only events where the lepton is identified as a muon, since this sample has a negligible contamination from QCD multijet events, contrary to the electron channel. A systematic uncertainty is derived from simulation to cover potential differences between the muon and the combined electron and muon samples.

The fit of the n_b distribution is also performed in the SB to determine the fraction $f_{t\bar{t}}^{\text{SB,CR}}$, since the $t\bar{t}$ contamination is significant and cannot be ignored. Examples of these fits are shown in Fig. 6.

The $t\bar{t}$ yields are then subtracted in the numerator and denominator when determining R^{CS} for the W +jets estimate:

$$R_{\text{data}}^{\text{CS,corr}}(n_{\text{jet}} \in [3, 4], n_b = 0, n_\mu = 1) = \frac{N_{\text{data}}^{\text{SB,SR}} - f_{t\bar{t}}^{\text{SB,CR}} \kappa_b R_{\text{data}}^{\text{CS}}(n_{\text{jet}} \in [4, 5], n_b \geq 1) N_{\text{data}}^{\text{SB,CR}}}{(1 - f_{t\bar{t}}^{\text{SB,CR}}) N_{\text{data}}^{\text{SB,CR}}}. \quad (12)$$

Similarly, a factor κ_W , defined in Eq. (13) and appearing in Eq. (14), corrects for a residual dependence of R_W^{CS} on the jet multiplicity; its typical values are 0.7 to 1.1. In addition, κ_W also provides the extrapolation from the muon to the electron channel:

$$\kappa_W = \frac{R_W^{\text{CS}}(n_{\text{jet}} \text{ as in MB}, n_b = 0, n_\ell = 1)}{R_{W+\text{other}}^{\text{CS}}(n_{\text{jet}} \in [3, 4], n_b = 0, n_\mu = 1)}, \text{ where } R_{\text{MC}}^{\text{CS}} = \frac{N_{\text{MC}}^{\text{SB,SR}}}{N_{\text{MC}}^{\text{SB,CR}}} \text{ and MC} \in [W, W+\text{other}]. \quad (13)$$

The final prediction of the W +jets background is then given by:

$$N_{\text{Pred},W}^{\text{MB,SR}} = \underbrace{\kappa_W R_{\text{data}}^{\text{CS,corr}}(n_{\text{jet}} \in [3, 4], n_b = 0, n_\mu = 1)}_{\text{transfer factor}} \underbrace{f_W^{\text{MB,CR}} N_{\text{data}}^{\text{MB,CR}}}_{W \text{ contribution in the control region}}. \quad (14)$$

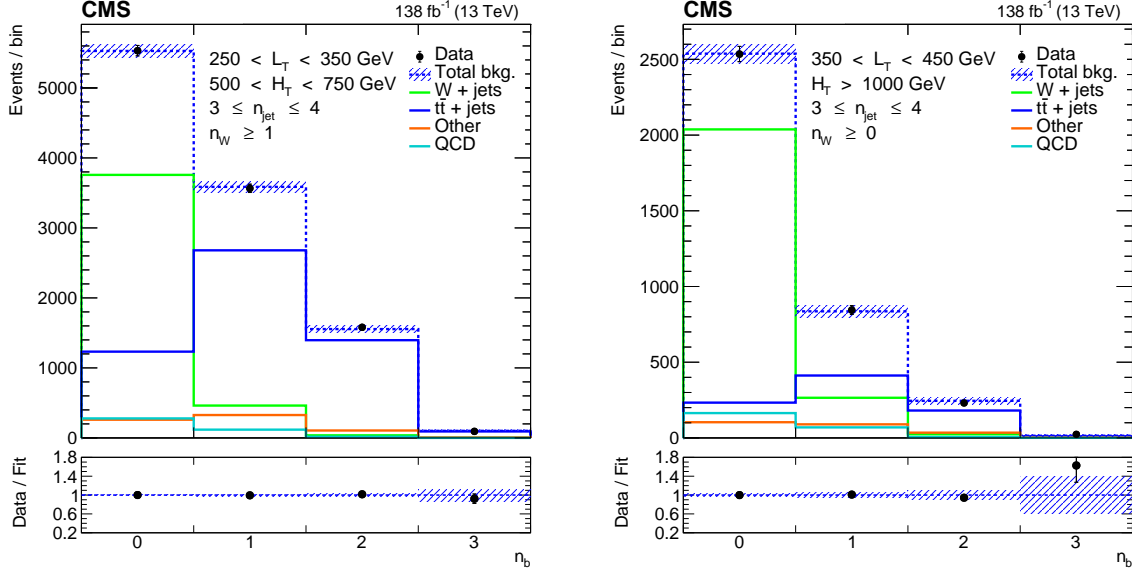


Figure 6: Results of fits to the n_b multiplicity for control regions for the muon channel and with the requirements $3 \leq n_{\text{jet}} \leq 4$, $250 < L_T < 350$ GeV, $500 < H_T < 750$ GeV, $n_W \geq 1$, $\Delta\phi < 1$ (left) and $3 \leq n_{\text{jet}} \leq 4$, $350 < L_T < 450$ GeV, $H_T > 1000$ GeV, $n_W \geq 0$, $\Delta\phi < 1$ (right). The shaded area shows the fit uncertainty of the total background.

6.3 Dilepton control region correction

The background prediction is sensitive to the extrapolation of R^{CS} from the low- n_{jet} SB to the MB regions with higher jet multiplicities. The R^{CS} values differ significantly for events with only one genuine lepton compared to events with two genuine leptons (mainly dileptonic $t\bar{t}$), where one lepton is not identified or lost. In the first case, the R^{CS} values are of the order 0.01–0.02, while for dileptonic events the value is around 0.5. In the latter case, the p_T^{miss} in the event is not only caused by the neutrino of a leptonically decaying W boson, but also by the second genuine lepton that is not identified, mostly because it is a hadronically decaying τ lepton leading to more neutrinos in the event, or because it is out of acceptance. This leads to more events in the high- $\Delta\phi$ region and a significantly higher R^{CS} . In general, the prediction is not affected by the different R^{CS} of the different processes, if the ratio of events with one genuine lepton to events with two genuine leptons (one lost or not identified) is the same for all n_{jet} regions.

Small differences can be corrected with an additional n_{jet} dependent correction factor that is applied to genuine simulated dilepton events. The high-purity dilepton events are transformed artificially into typical single-lepton events by removing the second lepton, as described in the following. The dilepton control sample is selected by requiring two leptons of opposite charge. In order to reduce the DY background in the multi-b analysis, the invariant mass of same-flavor leptons is required to be more than 10 GeV away from the Z boson mass peak. For the zero-b analysis, where the DY background is more important because of the zero b tag requirement, we allow only two leptons of different flavor. To simulate the feed-down of the dileptonic events into the single-lepton selection, one of the two leptons is removed from the event. Since these “lost leptons” are mainly from $\tau \rightarrow \text{hadrons} + \nu$ decays, we replace the removed lepton with a jet with $2/3$ of the original lepton’s p_T to model the typical visible energy of a τ lepton, accounting for the missing momentum caused by the neutrino from the τ lepton decay. In the next step L_T , $\Delta\phi$, and H_T values of the now “single-lepton” event (with the additional “jet”) are

recalculated. In order to maximize the number of events, no $\Delta\phi$ requirement is applied, and all events are used twice, with each reconstructed lepton being considered as the lost lepton.

In the events with one genuine lepton in the zero-b analysis, a change in the background composition (mainly $t\bar{t}$ and W +jets) could lead to a change of the correction factor. The size of this additional change is hard to determine and it is desirable to disentangle these two effects. In order to tackle this issue, we normalize these two backgrounds using weights extracted after performing the template fit on the b tag multiplicity.

The correction factor, w_{DL} , is determined as a function of n_{jet} for each event from a linear fit to the double ratio between data over MC yields for dilepton (transformed to “single-lepton”) and single-lepton events of the form:

$$w_{\text{DL}} = a + b(n_{\text{jet}} - \langle n_{\text{jet}} \rangle), \quad (15)$$

where a is the constant, b is the slope, and $\langle n_{\text{jet}} \rangle$ is the weighted mean. The correction factor is applied as a weight to all simulated events that are flagged as dileptonic from generator level information.

As an example, the evaluation using 2018 data is shown in Fig. 7. The jet multiplicity distributions are separately shown for single-lepton (after the single-lepton baseline selection but excluding the SRs) and for dilepton events, both for the multi-b and the zero-b analysis. Additionally, the fitted double ratio is provided.

The uncertainties in the templates are considered as a source of systematic uncertainty in the analysis and are discussed in Section 7.

6.4 Estimation of QCD multijet background

The QCD multijet events that pass the event selection typically have a reconstructed electron that originates from misidentified jets or from photon conversions in the inner detector. This background contribution is estimated from the yield of “anti-selected” electron candidates that pass looser identification and isolation requirements and fail the tighter criteria for selected electrons. Muons contribute naturally much less to this background, but are nevertheless studied in the same way. The transfer factor F_{SA} from the anti-selected to the selected lepton sample is extracted in a multijet-enriched control sample with zero b-tagged jets and three or four other jets and therefore fewer prompt leptons.

The estimation method applied here is very similar to the procedure developed in previous CMS analyses [98, 99]. It relies on the L_{P} variable, which reflects the effective lepton polarization in the W decay, defined as:

$$L_{\text{P}} = \frac{p_{\text{T}}^{\ell}}{p_{\text{T}}^{\text{W}}} \cos(\Delta\phi). \quad (16)$$

Here, $\Delta\phi$ is again the angle between the transverse components of the momenta of lepton and reconstructed W boson, as defined in Eq. (1). According to the simulation, the selected lepton events comprise a mixture of EW and QCD backgrounds. In contrast, the anti-selected electron events are clearly dominated by QCD background, as intended by the modified electron identification requirements. As shown in Fig. 8 for the electron channel, the EW background peaks around $L_{\text{P}} = 0$ and falls off towards higher values of L_{P} , while the QCD background peaks around unity. There is disagreement between the observed data and MC in the region of high L_{P} , however the effect of this disagreement will be negligible for the fit to estimate the QCD yields.

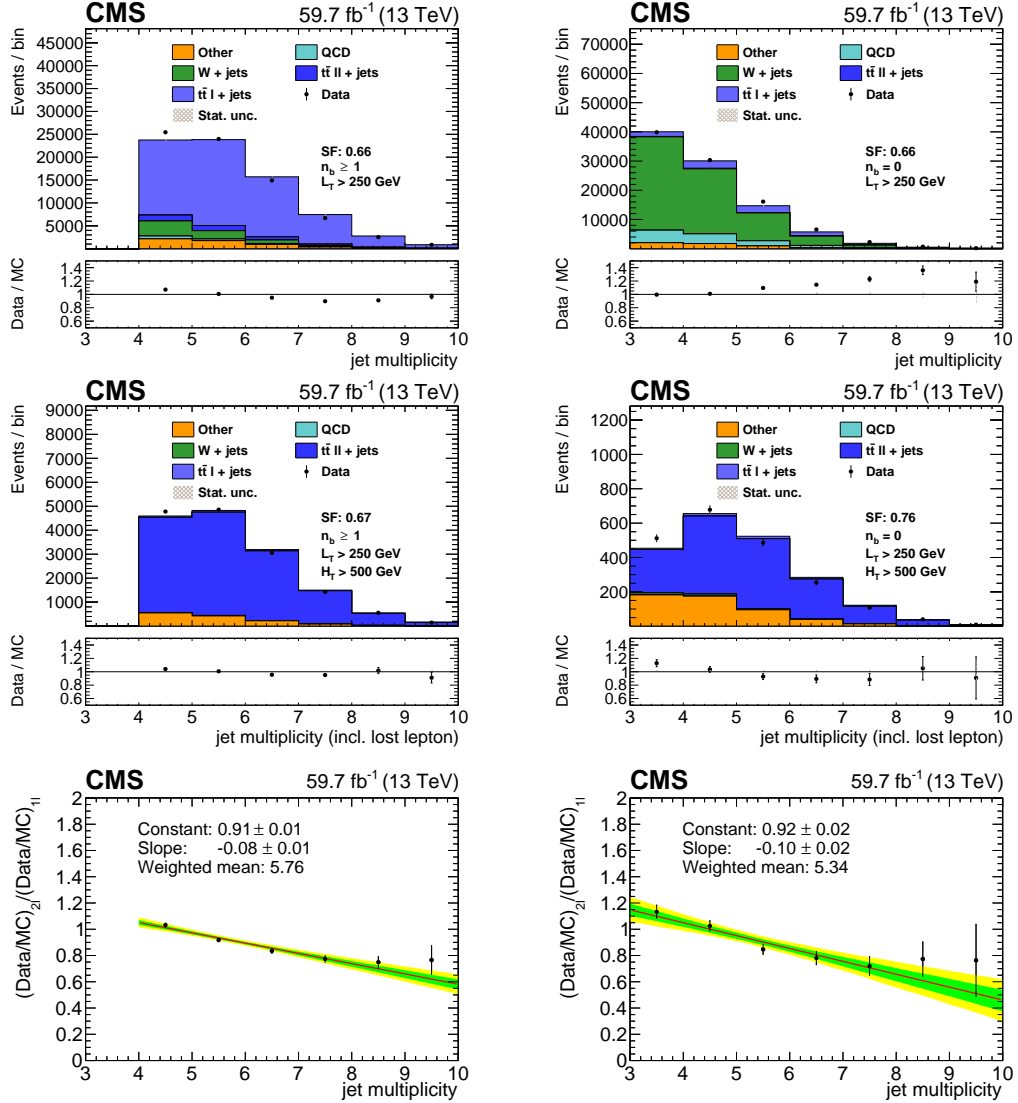


Figure 7: The upper row shows the jet multiplicity distribution after the single-lepton baseline selection excluding the SRs for the multi-b analysis (left) and for the zero-b analysis (right). The middle row contains the dilepton CRs, again for the multi-b analysis (left) and for the zero-b analysis (right). The simulation is normalized to data with the SF mentioned in the plot. The double ratio of the single-lepton and dilepton ratio between data and simulation together with fit results and their uncertainties is shown in the lower row for the multi-b (left) and the zero-b (right) analysis. The fits are performed for each data-taking year; 2018 is shown as an example.

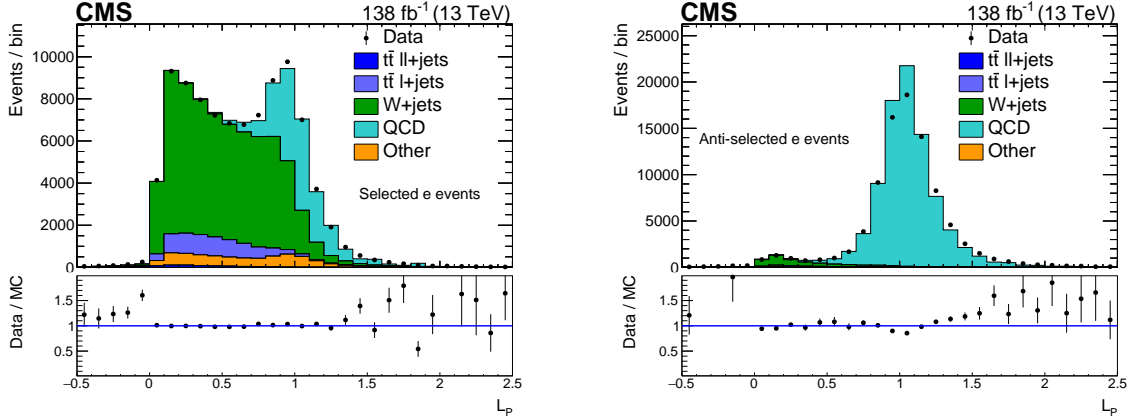


Figure 8: The prefit L_p distribution for selected (left) and anti-selected (right) electron candidates in the baseline QCD selection, with modified requirements of $n_{\text{jet}} \in [3, 4]$ and $n_b = 0$.

Therefore, the number of EW and QCD events can be determined with template fits in L_p to the selected and to the anti-selected lepton candidates. The shape of the templates is taken from the corresponding simulated samples. The ratio of QCD events in selected to anti-selected lepton events is then determined from data requiring zero b tags and three or four jets:

$$F_{\text{SA}}(L_T, n_b = 0, n_{\text{jet}} \in [3, 4]) = \frac{N_{\text{QCD selected}}^{\text{fit, data}}(L_T, n_b = 0, n_{\text{jet}} \in [3, 4])}{N_{\text{QCD anti-selected}}^{\text{fit, data}}(L_T, n_b = 0, n_{\text{jet}} \in [3, 4])}. \quad (17)$$

This ratio is calculated in bins of L_T , but inclusively in H_T , since the probability to misidentify jets as electrons is expected to be independent on the number of jets and H_T . Typically, the F_{SA} varies between 0.2 for smaller and 0.3 for large values of L_T . This ratio is finally used to predict the QCD background for the SR bins with higher jet or b-jet multiplicities bin by bin:

$$N_{\text{QCD selected}}^{\text{Pred}}(n_{\text{jet}}, n_b) = F_{\text{SA}}(L_T, n_b = 0, n_{\text{jet}} \in [3, 4]) N_{\text{QCD anti-selected}}^{\text{data}}(n_{\text{jet}}, n_b). \quad (18)$$

7 Systematic uncertainties

Our search results are subject to various systematic uncertainty sources related to the experimental apparatus and theoretical models. The uncertainties can influence the background estimations and/or modify the signal predictions. The impact of the uncertainties is evaluated individually for the multi-b and the zero-b analysis, and also separately for the $t\bar{t}$ and W+jets background predictions in the zero-b analysis. This is done by varying the yields of the MC simulation used to calculate the correction factors κ_{EW} or κ_b , $\kappa_{t\bar{t}}$ and κ_W , for various uncertainty sources split by year. The results are summarized in Tables 2 and 3, respectively. In addition, the impact of uncertainties on the yield predictions for two representative signal points for each analysis are shown in Tables 4 and 5. For the multi-b analysis, the p_T^{miss} uncertainty has a very high maximum value for T1tttt(2.2, 0.1) in one bin with low sensitivity to the signal.

One common large systematic uncertainty is given by the jet energy corrections, which are varied within their uncertainty [92] as a function of jet p_T and η , and these changes are propagated to all observables. The SF related to the efficiencies for identifying leptons as well as b quark jets, and the misidentification of the c quark, light quark, or gluon jets are scaled up and down according to their uncertainties in the efficiency. The uncertainty in the pileup is determined by varying the inelastic pp cross-section of 69 mb by $\pm 5\%$ [100]. All these uncertainties apply to both the background prediction and the signal yield.

Table 2: Summary of systematic uncertainties in the background prediction for the multi-b analysis. For each uncertainty source, the median, minimal (min), and maximal (max) impact on the total background prediction is shown in order of decreasing importance, where these quantities refer to the set of MB SR bins.

Uncertainty source	Total background median [min, max] [%]
Jet energy corrections	3.8 [0.2, 36.3]
QCD multijet	3.8 [0.8, 71.0]
$t\bar{t}V$ cross sections	2.8 [0.1, 22.6]
ISR modeling	2.3 [0.4, 20.3]
Pileup modeling	2.3 [0.1, 18.6]
Dileptonic correction	2.2 [0.4, 12.3]
$t\bar{t}$ cross section	1.6 [0.1, 23.7]
W+jets polarization	0.6 [0.1, 4.4]
b tagging (efficiency)	0.6 [0.1, 5.7]
W+jets cross section	0.4 [0.1, 7.7]
b tagging (misidentification)	0.3 [0.1, 8.4]
Lepton efficiency	0.2 [0.1, 1.6]

Table 3: Summary of systematic uncertainties in the background prediction for the zero-b analysis. For each uncertainty source, the median, minimal (min), and maximal (max) impact on the $t\bar{t}$, W+jets, and total background prediction is shown in order of decreasing importance for the total background, where these quantities refer to the set of MB SR bins.

Uncertainty source	$t\bar{t}$ median [min, max] [%]	W+jets median [min, max] [%]	Total background median [min, max] [%]
QCD multijet	—	—	5.2 [1.5, 27.6]
$t\bar{t}V$ cross sections	0.9 [0.2, 5.3]	0.3 [0.1, 2.1]	4.0 [1.0, 19.6]
Jet energy corrections	1.4 [0.1, 34.4]	1.2 [0.1, 22.0]	3.5 [0.5, 40.5]
Pileup modeling	0.5 [0.1, 5.5]	0.6 [0.1, 4.8]	1.2 [0.1, 13.1]
Dileptonic correction	2.0 [0.2, 13.7]	0.1 [0.1, 0.9]	0.8 [0.1, 4.7]
W+jets cross section	0.6 [0.1, 2.6]	1.5 [0.1, 13.7]	0.7 [0.1, 4.5]
b tagging (efficiency)	0.3 [0.1, 2.7]	0.1 [0.1, 1.8]	0.6 [0.2, 4.6]
W+jets polarization	0.2 [0.1, 2.9]	0.8 [0.1, 7.6]	0.4 [0.1, 4.1]
Lepton efficiency	0.1 [0.1, 1.4]	0.1 [0.1, 1.6]	0.4 [0.1, 2.3]
$t\bar{t}$ cross section	1.3 [0.1, 10.3]	—	0.3 [0.1, 3.2]
Integrated luminosity	—	—	0.3 [0.1, 1.0]
ISR modeling	0.5 [0.1, 14.1]	—	0.1 [0.1, 4.4]
b tagging (misidentification)	0.1 [0.1, 0.5]	0.1 [0.1, 0.3]	0.1 [0.1, 0.7]

The integrated luminosities of the 2016, 2017, and 2018 data-taking periods are individually measured with uncertainties in the 1.2–2.5% range [101–103], while the total integrated luminosity has an uncertainty of 1.6%.

Changes in the polarization of W bosons can affect the $\Delta\phi$ variable. Thus, events are reweighted using the factor $w = 1 + \alpha(1 - \cos\theta^*)^2$, where θ^* is the angle between the charged lepton and W boson in the W boson rest frame. In W+jets events, we take α to be 0.1, guided by the theoretical uncertainty and measurements found in Refs. [98, 104–106]. For $t\bar{t}$ +jets events, we take $\alpha = 0.05$ [107–110]. For W+jets events, where the initial state can have different polarizations for W^+ and W^- bosons, we take as uncertainty the larger change in κ resulting from reweighting

Table 4: Summary of the main systematic uncertainties in the signal prediction for the multi-b analysis, for two representative combinations of (gluino, neutralino) masses with large (2.2, 0.1) TeV and small (1.8, 1.3) TeV mass differences. For each uncertainty source, the median, minimal (min), and maximal (max) impact on the total background prediction is shown in order of decreasing importance for the T1tttt(1.8, 1.3) TeV signal, where these quantities refer to the set of MB SR bins.

Uncertainty source	T1tttt(1.8, 1.3) TeV median [min, max] [%]	T1tttt(2.2, 0.1) TeV median [min, max] [%]
t tagging	10.0 [10.0, 10.0]	10.0 [10.0, 10.0]
Jet energy corrections	10.4 [0.1, 62.0]	8.8 [0.1, 58.8]
p_T^{miss}	8.4 [1.0, 73.3]	4.2 [0.1, 129.2]
ISR modeling	4.7 [0.1, 50.9]	6.2 [0.1, 27.1]
b tagging (efficiency)	4.6 [0.1, 15.9]	7.3 [0.1, 26.9]
Integrated luminosity	1.6 [1.6, 1.6]	1.6 [1.6, 1.6]
b tagging (misidentification)	0.5 [0.1, 8.9]	0.6 [0.1, 7.4]

Table 5: Summary of the main systematic uncertainties in the signal prediction for the zero-b analysis, for two representative combinations of (gluino, neutralino) masses with large (2.2, 0.1) TeV and small (1.8, 1.3) TeV mass differences. For each uncertainty source, the median, minimal (min), and maximal (max) impact on the total background prediction is shown in order of decreasing importance for the T5qqqqWW(1.8, 1.3) TeV signal, where these quantities refer to the set of MB SR bins.

Uncertainty source	T5qqqqWW(1.8, 1.3) TeV median [min, max] [%]	T5qqqqWW(2.2, 0.1) TeV median [min, max] [%]
W boson tagging	10.0 [10.0, 10.0]	10.0 [10.0, 10.0]
Jet energy corrections	6.2 [0.8, 72.5]	5.1 [0.1, 50.0]
p_T^{miss}	4.0 [0.1, 28.4]	4.9 [0.1, 63.9]
ISR modeling	1.8 [0.1, 11.3]	1.7 [0.1, 14.8]
Integrated luminosity	1.6 [1.6, 1.6]	1.6 [1.6, 1.6]
b tagging (efficiency)	0.5 [0.2, 5.9]	1.3 [0.2, 6.0]
b tagging (misidentification)	0.2 [0.1, 0.9]	0.4 [0.1, 1.1]

only the W^+ bosons in the sample, and from reweighting all W bosons.

While the W +jets and $t\bar{t}$ backgrounds are estimated from data, a change in their relative contribution can lead to changes in the R^{CS} at low jet multiplicities of the SB. Therefore, the inclusive W +jets and $t\bar{t}$ cross sections are varied by 30% above and below the nominal value [111] to account for possible biases in the estimation of the background composition, which only affects the calculation of the κ factors. The small contribution of $t\bar{t}$ produced with an additional vector boson ($t\bar{t}V$) is varied by 100% to account for the uncertainty in the theoretical prediction. Uncertainties in the signal cross section are shown as explicit variations of the mass limits (Section 9).

The QCD uncertainty includes the statistical uncertainties in the anti-selected region. As F_{SA} is calculated for events with 3–4 jets, we apply an additional relative uncertainty that is larger for SR bins with higher jet multiplicities. An uncertainty of 30% for events with 6–8 jets, or 50% for events with least 9 jets in the multi-b analysis is applied on the QCD background estimate. For the zero-b analysis, we take an uncertainty of 15% for events with 5 jets, 30% for events with

6–7 jets, and 50% for events with at least 8 jets.

Since we consider a signal with multiple top quarks (W bosons) in the multi- b (zero- b) analysis, the related tagging uncertainties have been investigated. The taggers are described in detail in Section 4. The background estimation is not sensitive to details of the t and W boson tagging performance, therefore a systematic uncertainty is only assigned for the signal efficiency. The systematic uncertainties in the t tagging efficiency and mistagging rate are estimated as follows: The relative yields of events with different t tag multiplicities are used to extract an overall efficiency and mistagging rate. A difference of 5% is observed, and the systematic uncertainty is taken to be twice this quantity, namely 10%. For W boson tagging, the efficiency and mistagging rates are extracted from a full comparison of data and simulation. A total uncertainty of 10% is found to account for all differences between data and simulation.

The SF applied to correct the ISR in signal samples and 2016 $t\bar{t}$, with values typically around 0.94, is varied by 4–5% (Section 3).

Because the signal samples use fast simulation, an additional p_T^{miss} uncertainty is taken into account. The analysis is performed twice, once using the generated and once using the reconstructed p_T^{miss} for signal events. A flat uncertainty equal to one-half the difference between the acceptances is applied.

Lastly, systematic uncertainties related to the dileptonic correction explained in Section 6.3 have to be taken into account. The systematic variations around that new central value are determined by varying the fit to the double ratio by the following uncertainties: the variation of the constant value a is extracted as the quadratic sum of the deviation of the central value of a from unity and by the uncertainty in a that is extracted from the fit itself. The variation of the slope b is determined as the quadratic sum of the deviation of b from zero and the uncertainty in b as given by the fit.

8 Results

The observed data yields and the predicted background contributions for the multi- b analysis are given in Table 6 and shown in Fig. 9 for the MB SR for the combination of all three data-taking years. Good agreement is observed for almost all search bins, except for the last bin where two events are observed, against an expected value of 0.24 ± 0.16 . The observed limit is about one standard deviation lower than expected, because of the number of excess events in the last search bin.

Table 7 and Fig. 10 show the background predictions for the zero- b analysis and the data yields in the MB SR. Here, we observe good agreement in almost all bins as well, and a deviation from the prediction is observed only for bins that are dominated by the background. Namely, the bins G2b, H3a, and I3a, among the 50 zero- b bins, contain more observed events than expected by at least one standard deviation.

9 Interpretation

To evaluate exclusion limits on the simplified SUSY models considered in this search, a likelihood function is defined that includes all SB and MB CRs and SRs. For the multi- b analysis, the measurement is performed for each set of four bins (SB CR, SB SR, MB CR and MB SR), as defined for the R^{CS} method in Section 6.1. The number of entries in the bins are modeled by a product of Poisson distributions taking into account that the R^{CS} method represents a factoriza-

Table 6: Observed number of events in the MB SR bins of the multi-b analysis, together with the predicted yields for background and two T1tttt ($m_{\tilde{g}}, m_{\tilde{\chi}_1^0}$) signal points. All bins are defined with $\Delta\phi > 0.75$.

n_{jet}	n_b	L_T [GeV]	H_T [GeV]	n_t	Bin name	T1tttt signal events		Predicted background events	Observed events		
						(1.8, 1.3) TeV	(2.2, 0.1) TeV				
[6, 8]	1	[250, 450]	[500, 1500]	1	A1a	1.2 ± 0.1	<0.1	576 ± 29	570		
				≥ 2	A1b	0.07 ± 0.02	<0.1	13 ± 2	14		
				1	A2a	<0.1	0.01 ± 0.01	47 ± 7	42		
				≥ 2	A2b	<0.1	0.04 ± 0.01	5 ± 1	3		
		[450, 600]	>500	1	A3a	0.44 ± 0.06	0.04 ± 0.01	31 ± 6	16		
				≥ 2	A3b	0.03 ± 0.02	0.06 ± 0.01	1.0 ± 0.3	1		
			>600	>500	1	A4a	0.18 ± 0.04	0.44 ± 0.02	7 ± 2	8	
				≥ 2	A4b	<0.1	0.48 ± 0.02	1.0 ± 0.5	0		
	2	[250, 450]	[500, 1500]	1	B1a	2.3 ± 0.1	0.01 ± 0.01	532 ± 26	586		
				≥ 2	B1b	0.28 ± 0.04	0.01 ± 0.01	16 ± 2	19		
				1	B2a	<0.1	0.03 ± 0.01	30 ± 5	34		
				≥ 2	B2b	<0.1	0.06 ± 0.01	3.4 ± 0.8	1		
		[450, 600]	>500	1	B3a	1.0 ± 0.1	0.07 ± 0.01	27 ± 6	34		
				≥ 2	B3b	0.06 ± 0.02	0.09 ± 0.01	1.1 ± 0.5	2		
			>600	>500	1	B4a	0.37 ± 0.05	0.67 ± 0.03	6.2 ± 1.6	6	
				≥ 2	B4b	0.07 ± 0.02	0.80 ± 0.03	0.23 ± 0.08	0		
≥ 3	[250, 450]	[500, 1500]	1	C1a	3.0 ± 0.1	0.01 ± 0.01	115 ± 7	105			
			≥ 2	C1b	0.43 ± 0.06	<0.1	6 ± 1	3			
			1	C2a	0.01 ± 0.01	0.03 ± 0.01	7 ± 2	10			
			≥ 2	C2b	<0.1	0.07 ± 0.01	1.0 ± 0.4	2			
	[450, 600]	>500	1	C3a	1.1 ± 0.1	0.06 ± 0.01	5 ± 1	4			
			≥ 2	C3b	0.24 ± 0.04	0.10 ± 0.01	0.63 ± 0.43	0			
		>600	>500	1	C4a	0.42 ± 0.05	0.67 ± 0.02	1.4 ± 0.4	4		
			≥ 2	C4b	0.05 ± 0.02	0.76 ± 0.03	0.05 ± 0.04	0			
≥ 9	1	[250, 450]	[500, 1500]	1	D1a	0.62 ± 0.06	<0.1	32 ± 3	26		
				≥ 2	D1b	0.12 ± 0.03	<0.1	2.1 ± 0.6	4		
				1	D2a	0.02 ± 0.01	0.01 ± 0.01	6 ± 1	11		
				≥ 2	D2b	0.02 ± 0.01	0.02 ± 0.01	1.0 ± 0.3	2		
		[450, 600]	>500	≥ 1	D3	0.34 ± 0.05	0.04 ± 0.01	2.3 ± 0.6	2		
				≥ 1	D4	0.23 ± 0.04	0.40 ± 0.02	0.6 ± 0.3	0		
			2	[250, 450]	[500, 1500]	1	E1a	1.5 ± 0.1	0.01 ± 0.01	35 ± 3	35
						≥ 2	E1b	0.55 ± 0.06	<0.1	3.2 ± 0.7	2
	1	E2a				0.05 ± 0.02	0.02 ± 0.01	8 ± 2	6		
	≥ 2	E2b				0.04 ± 0.02	0.05 ± 0.01	1.0 ± 0.4	2		
	[450, 600]	>500	1	E3a	0.75 ± 0.07	0.04 ± 0.01	1.7 ± 0.5	1			
			≥ 2	E3b	0.19 ± 0.03	0.06 ± 0.01	0.2 ± 0.1	0			
		>600	>500	1	E4a	0.50 ± 0.05	0.30 ± 0.02	0.9 ± 0.4	1		
			≥ 2	E4b	0.21 ± 0.04	0.55 ± 0.02	0.06 ± 0.04	0			
	≥ 3	[250, 450]	[500, 1500]	1	F1a	3.2 ± 0.1	0.01 ± 0.01	13 ± 2	7		
				≥ 2	F1b	1.27 ± 0.08	<0.1	2.4 ± 0.8	2		
1				F2a	0.04 ± 0.02	0.03 ± 0.01	4 ± 1	0			
≥ 2				F2b	0.07 ± 0.02	0.09 ± 0.01	0.7 ± 0.3	0			
[450, 600]		>500	≥ 1	F3	1.7 ± 0.1	0.16 ± 0.01	1.1 ± 0.4	2			
			≥ 1	F4	1.0 ± 0.1	1.30 ± 0.03	0.24 ± 0.16	2			

Table 7: Observed number of events in the MB SR bins of the zero-b analysis, together with the predicted yields for background and two T5qqqqWW ($m_{\tilde{g}}, m_{\tilde{\chi}_1^0}$) signal points.

n_{jet}	L_T [GeV]	H_T [GeV]	$\Delta\phi$	n_W	Bin name	T5qqqqWW signal events		Predicted background events	Observed events	
						(1.8, 1.3) TeV	(2.2, 0.1) TeV			
5	[250, 350]	[500, 750]	>1	0	G0a	1.2 ± 0.1	<0.1	342 ± 24	333	
				≥ 1	G0b	0.46 ± 0.08	<0.1	70 ± 8	77	
				0	G1a	0.35 ± 0.07	0.03 ± 0.01	292 ± 22	304	
				≥ 1	G1b	0.14 ± 0.04	0.02 ± 0.01	69 ± 10	62	
	[350, 450]	[500, 750]	>1	0	G2a	1.8 ± 0.2	<0.1	71 ± 8	63	
				≥ 1	G2b	0.60 ± 0.09	<0.1	14 ± 5	25	
				0	G3a	0.44 ± 0.08	0.04 ± 0.01	66 ± 8	44	
				≥ 1	G3b	0.24 ± 0.06	0.03 ± 0.01	14 ± 4	13	
	[450, 650]	[500, 750]	>0.75	0	G4a	2.1 ± 0.2	<0.1	52 ± 7	45	
				≥ 1	G4b	1.1 ± 0.1	<0.1	12 ± 3	9	
				0	G5a	0.9 ± 0.1	0.03 ± 0.01	42 ± 6	35	
				≥ 1	G5b	0.35 ± 0.07	<0.1	10 ± 3	6	
		[750, 1250]	>750	0	G6a	<0.1	0.17 ± 0.02	16 ± 3	19	
				≥ 1	G6b	<0.1	0.13 ± 0.02	3 ± 1	3	
				0	G7a	1.3 ± 0.1	0.13 ± 0.02	33 ± 8	32	
				≥ 1	G7b	0.30 ± 0.06	0.04 ± 0.01	7 ± 2	8	
	>650	[500, 1250]	>0.5	0	G8a	0.15 ± 0.05	1.78 ± 0.07	11 ± 3	8	
				≥ 1	G8b	0.04 ± 0.02	1.08 ± 0.05	0.6 ± 0.4	2	
				0	G9a	0.23 ± 0.06	0.05 ± 0.01	121 ± 11	121	
				≥ 1	G9b	0.18 ± 0.05	0.02 ± 0.01	29 ± 5	21	
[6, 7]	[250, 350]	[500, 1000]	>1	0	H1a	2.6 ± 0.2	<0.1	281 ± 22	292	
				≥ 1	H1b	1.3 ± 0.1	<0.1	71 ± 9	71	
				0	H2a	0.23 ± 0.06	0.05 ± 0.01	121 ± 11	121	
				≥ 1	H2b	0.18 ± 0.05	0.02 ± 0.01	29 ± 5	21	
	[350, 450]	[500, 1000]	>1	0	H3a	3.1 ± 0.2	<0.1	51 ± 6	71	
				≥ 1	H3b	1.6 ± 0.2	0.01 ± 0.01	12 ± 3	15	
				0	H4a	0.31 ± 0.07	0.09 ± 0.01	31 ± 7	21	
				≥ 1	H4b	0.12 ± 0.04	0.08 ± 0.01	6 ± 2	6	
	[450, 650]	[500, 750]	>0.75	0	H5a	3.1 ± 0.2	<0.1	19 ± 4	17	
				≥ 1	H5b	1.6 ± 0.2	<0.1	5 ± 2	9	
				0	H6a	2.8 ± 0.2	0.01 ± 0.01	29 ± 4	18	
				≥ 1	H6b	1.4 ± 0.1	<0.1	7 ± 2	4	
		[750, 1250]	>1250	0	H7a	0.4 ± 0.07	0.45 ± 0.03	15 ± 3	14	
				≥ 1	H7b	0.2 ± 0.05	0.33 ± 0.03	3 ± 1	1	
				0	H8a	2.5 ± 0.2	0.09 ± 0.01	13 ± 3	17	
				≥ 1	H8b	0.9 ± 0.1	0.05 ± 0.01	4 ± 1	4	
	>650	[500, 1250]	>0.5	0	H9a	0.8 ± 0.1	3.9 ± 0.1	9 ± 3	6	
				≥ 1	H9b	0.34 ± 0.07	2.44 ± 0.08	2 ± 1	1	
				0	H10a	0.8 ± 0.1	<0.1	23 ± 5	25	
				≥ 1	H10b	0.33 ± 0.07	<0.1	7 ± 3	5	
≥ 8	[250, 350]	[500, 1000]	>1	0	I1a	0.8 ± 0.1	<0.1	23 ± 5	25	
				≥ 1	I1b	0.33 ± 0.07	<0.1	7 ± 3	5	
				0	I2a	0.30 ± 0.07	0.04 ± 0.01	22 ± 5	23	
				≥ 1	I2b	0.16 ± 0.05	0.01 ± 0.01	8 ± 2	12	
	[350, 450]	[500, 1000]	>1	0	I3a	0.8 ± 0.1	<0.1	3.0 ± 0.7	10	
				≥ 1	I3b	0.36 ± 0.07	<0.1	1.1 ± 0.4	0	
				0	I4a	0.57 ± 0.09	0.07 ± 0.01	5 ± 1	5	
				≥ 1	I4b	0.36 ± 0.07	0.06 ± 0.01	3 ± 1	2	
	[450, 650]	[500, 1250]	>0.75	0	I5a	1.5 ± 0.1	<0.1	3.4 ± 0.9	4	
				≥ 1	I5b	1.0 ± 0.1	<0.1	0.5 ± 0.3	1	
				0	I6a	0.40 ± 0.07	0.26 ± 0.03	2.6 ± 0.8	2	
				≥ 1	I6b	0.18 ± 0.05	0.17 ± 0.02	0.5 ± 0.3	2	
		>650	[500, 1250]	>0.5	≥ 0	I7	1.4 ± 0.1	0.02 ± 0.01	1.5 ± 0.6	2
						I8	1.4 ± 0.1	3.58 ± 0.09	1.5 ± 0.7	1

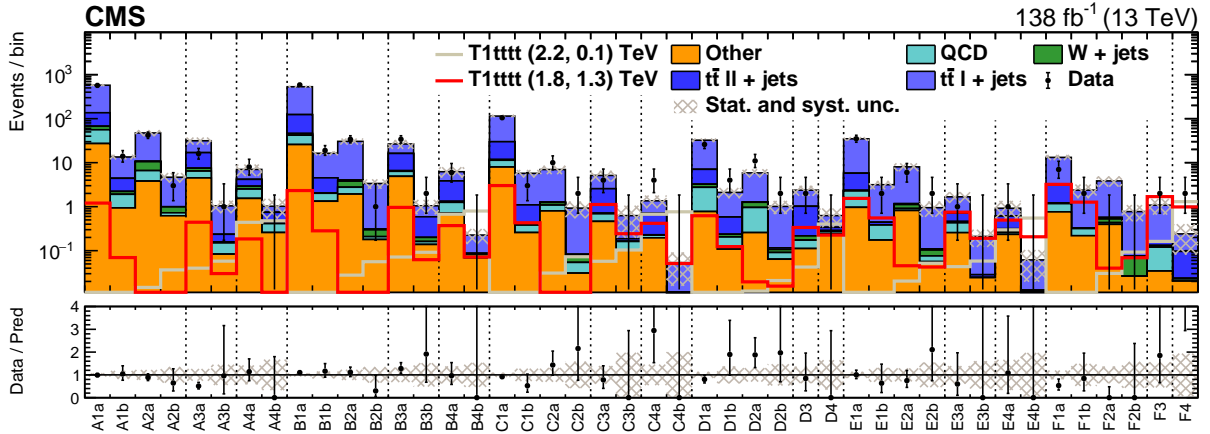


Figure 9: Observed event yields in the MB SRs of the multi-b analysis compared to signal and background predictions. The relative fraction of the different SM EW background contributions determined in simulation is shown by the stacked, colored histograms, normalized so that their sum is equal to the background estimated using data control regions. The QCD background is predicted using the L_P method. The signal is shown for two representative combinations of (gluino, neutralino) masses with large (2.2, 0.1) TeV and small (1.8, 1.3) TeV mass differences.

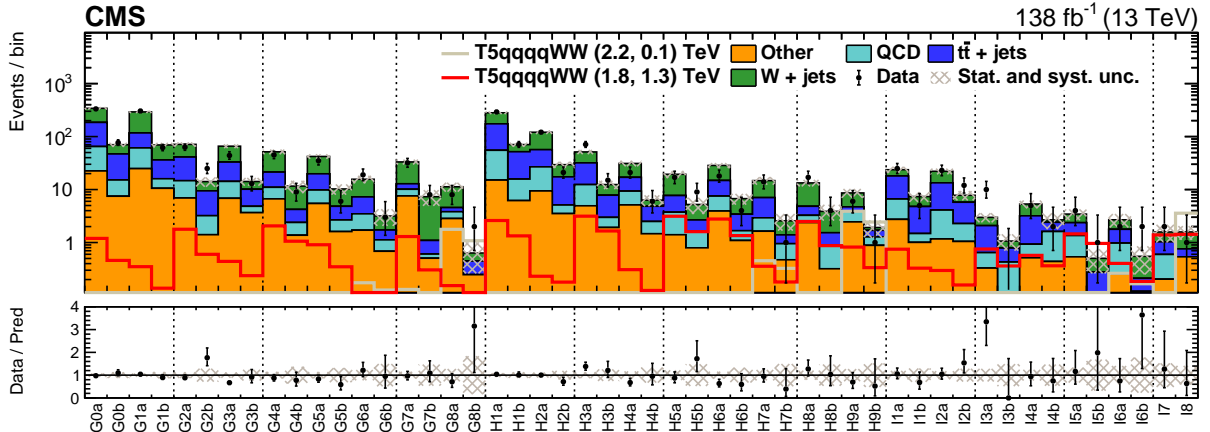


Figure 10: Observed event yields in the MB SRs of the zero-b analysis compared to signal and background predictions. The W+jets, $t\bar{t}$, and QCD predictions are extracted from data control samples, while the other background contributions are estimated from simulation. The signal is shown for two representative combinations of (gluino, neutralino) masses with large (2.2, 0.1) TeV and small (1.8, 1.3) TeV mass differences.

tion approach, which constrains the rate parameter for the background estimate in the signal region. Multijet background and rare processes are treated as independent contributions. The systematic uncertainties enter the likelihood as nuisance parameters and are taken into account as a product of log-normal distributions. For the zero-b analysis, the bins are defined in Section 6.1. The template fit on the n_b distributions is performed separately. Thus, only the SB' CR, SB' SR, SB SR and MB SR search bins enter the likelihood. The different constraints on the rate parameters implied by the extended R^{CS} method are taken into account in a similar way and the systematic uncertainties are again modeled by log-normal distributions. We set upper limits on the production cross section at 95% confidence level (CL). These are estimated with the modified frequentist CL_s method [112, 113] using the asymptotic approximation [114]. The CL_s method is used with the test statistic $q_\mu = -2 \ln \lambda_\mu$, where λ_μ refers to the ratio of the maximized likelihood for a given signal strength μ to the unconditional likelihood maximized

for all parameters, including μ . The $\tilde{g}\tilde{g}$ pair production cross section is calculated at approximate NNLO and NNLL accuracy, and exclusion limits are set as a function of the $(m_{\tilde{g}}, m_{\tilde{\chi}_1^0})$ hypothesis.

For the T1tttt model, which describes gluino pair production with each gluino decaying to a $t\bar{t}$ pair and a $\tilde{\chi}_1^0$, the cross section limits are obtained using the multi-b analysis. They are shown in Fig. 11 (left) as functions of $m_{\tilde{g}}$ and $m_{\tilde{\chi}_1^0}$, assuming branching fractions of 100%. The observed limit is about one standard deviation lower than the expected one, which is caused by the observation of two events in the last bin, while only 0.24 ± 0.16 events are expected.

The results of the zero-b analysis are interpreted in the T5qqqqWW model, in which pair-produced gluinos decay to a (light) quark-antiquark pair and a chargino, which further decays to a W boson and the $\tilde{\chi}_1^0$. The observed limit, shown in Fig. 11 (right), agrees with the expected limit over most of the mass range.

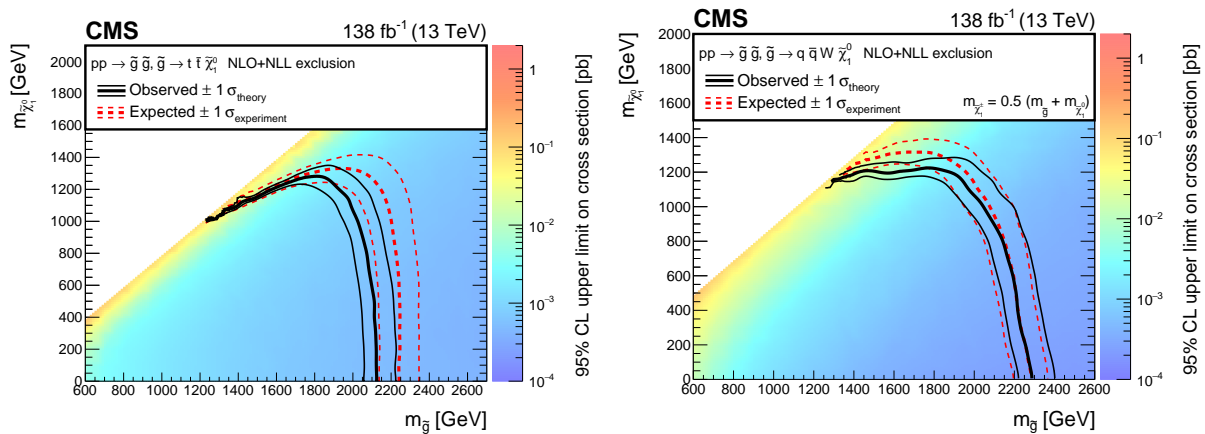


Figure 11: Cross section limits at 95% CL for the T1tttt (left) and for the T5qqqqWW (right) model, as functions of the gluino and LSP masses, assuming a branching fraction of 100%. The mass of the intermediate chargino is taken to be halfway between the gluino and the neutralino masses. The solid black (dashed red) lines correspond to the observed (expected) mass limits, with the thicker lines representing the central values and the thinner lines representing the $\pm 1\sigma$ uncertainty bands related to the theoretical (experimental) uncertainties.

10 Summary

A search for supersymmetry has been performed using a sample of proton-proton collisions at $\sqrt{s} = 13$ TeV corresponding to an integrated luminosity of 138 fb^{-1} , recorded by the CMS experiment in 2016–2018. Events with a single charged lepton (electron or muon) and multiple jets are selected. Top quark and W boson identification algorithms based on machine-learning techniques are employed to suppress the main background contributions in the analysis. Various exclusive search regions are defined that differ in the number of jets, the number of jets identified as stemming from b quarks, the number of hadronically decaying top quarks or W bosons, the scalar sum of all jet transverse momenta, and the scalar sum of the missing transverse momentum and the transverse momentum of the lepton.

To reduce the main background processes from $t\bar{t}$ and W+jets production, the presence of a lepton produced in the leptonic decay of a W boson in the event is exploited. Under the hypothesis that all of the missing transverse momentum in the event originates from the neutrino

produced in a leptonic W boson decay, the W boson momentum is calculated. The requirement of a large azimuthal angle between the directions of the lepton and of the reconstructed W boson decaying leptonically, notably reduces the background contributions.

The event yields observed in data are consistent with the expectations from the SM processes, which are estimated using control samples in data. Exclusion limits on the supersymmetric particle masses in the context of two simplified models of gluino pair production are evaluated.

For the T1tttt simplified model, where each gluino decays to a top quark-antiquark pair and the lightest neutralino, the excluded gluino masses reach up to 2130 GeV, while the excluded neutralino masses reach up to 1270 GeV. This result extends the exclusion limit on gluino (neutralino) masses from a previous CMS search [19] by about 320 (170) GeV.

The second simplified model, T5qqqqWW, also targets gluino pair production, but with decays to a light-flavor quark-antiquark pair and a chargino, which decays to a W boson and the lightest neutralino. The chargino mass in this decay channel is assumed to be $m_{\tilde{\chi}_1^\pm} = 0.5(m_{\tilde{g}} + m_{\tilde{\chi}_1^0})$. The excluded gluino masses reach up to 2280 GeV, while the excluded neutralino masses reach up to 1220 GeV. This corresponds to an improvement on gluino (neutralino) masses by about 380 (270) GeV in comparison with the previous result [19], extending the existing limit from ATLAS [13] on the neutralino mass in the compressed region by about 150 GeV.

References

- [1] J. Wess and B. Zumino, "A Lagrangian model invariant under supergauge transformations", *Phys. Lett. B* **49** (1974) 52, doi:10.1016/0370-2693(74)90578-4.
- [2] P. Fayet and S. Ferrara, "Supersymmetry", *Phys. Rept.* **32** (1977) 249, doi:10.1016/0370-1573(77)90066-7.
- [3] R. Barbieri, S. Ferrara, and C. A. Savoy, "Gauge models with spontaneously broken local supersymmetry", *Phys. Lett. B* **119** (1982) 343, doi:10.1016/0370-2693(82)90685-2.
- [4] H. P. Nilles, "Supersymmetry, supergravity and particle physics", *Phys. Rept.* **110** (1984) 1, doi:10.1016/0370-1573(84)90008-5.
- [5] H. E. Haber and G. L. Kane, "The search for supersymmetry: probing physics beyond the standard model", *Phys. Rept.* **117** (1985) 75, doi:10.1016/0370-1573(85)90051-1.
- [6] S. P. Martin, "A supersymmetry primer", *Adv. Ser. Direct. High Energy Phys.* **21** (2010) 1, doi:10.1142/9789814307505_0001, arXiv:hep-ph/9709356.
- [7] G. R. Farrar and P. Fayet, "Phenomenology of the production, decay, and detection of new hadronic states associated with supersymmetry", *Phys. Lett. B* **76** (1978) 575, doi:10.1016/0370-2693(78)90858-4.
- [8] N. Arkani-Hamed et al., "MARMOSSET: The path from LHC data to the new standard model via on-shell effective theories", 2007. arXiv:hep-ph/0703088.
- [9] J. Alwall, P. Schuster, and N. Toro, "Simplified models for a first characterization of new physics at the LHC", *Phys. Rev. D* **79** (2009) 075020, doi:10.1103/PhysRevD.79.075020, arXiv:0810.3921.

- [10] J. Alwall, M.-P. Le, M. Lisanti, and J. G. Wacker, “Model-independent jets plus missing energy searches”, *Phys. Rev. D* **79** (2009) 015005, doi:10.1103/PhysRevD.79.015005, arXiv:0809.3264.
- [11] D. Alves et al., “Simplified models for LHC new physics searches”, *J. Phys. G* **39** (2012) 105005, doi:10.1088/0954-3899/39/10/105005, arXiv:1105.2838.
- [12] CMS Collaboration, “Interpretation of searches for supersymmetry with simplified models”, *Phys. Rev. D* **88** (2013) 052017, doi:10.1103/PhysRevD.88.052017, arXiv:1301.2175.
- [13] ATLAS Collaboration, “Search for squarks and gluinos in final states with one isolated lepton, jets, and missing transverse momentum at $\sqrt{s} = 13$ TeV with the ATLAS detector”, *Eur. Phys. J. C* **81** (2021) 600, doi:10.1140/s10052-021-09344-w, arXiv:2101.01629.
- [14] ATLAS Collaboration, “Search for squarks and gluinos in events with an isolated lepton, jets, and missing transverse momentum at $\sqrt{s} = 13$ TeV with the ATLAS detector”, *Phys. Rev. D* **96** (2017) 112010, doi:10.1103/PhysRevD.96.112010, arXiv:1708.08232.
- [15] ATLAS Collaboration, “Search for supersymmetry in final states with missing transverse momentum and multiple b-jets in proton-proton collisions at $\sqrt{s} = 13$ TeV with the ATLAS detector”, *JHEP* **06** (2018) 107, doi:10.1007/JHEP06(2018)107, arXiv:1711.01901.
- [16] ATLAS Collaboration, “Search for gluinos in events with an isolated lepton, jets and missing transverse momentum at $\sqrt{s} = 13$ TeV with the ATLAS detector”, *Eur. Phys. J. C* **76** (2016) 565, doi:10.1140/epjc/s10052-016-4397-x, arXiv:1605.04285.
- [17] ATLAS Collaboration, “Search for pair production of gluinos decaying via stop and sbottom in events with b-jets and large missing transverse momentum in pp collisions at $\sqrt{s} = 13$ TeV with the ATLAS detector”, *Phys. Rev. D* **94** (2016) 032003, doi:10.1103/PhysRevD.94.032003, arXiv:1605.09318.
- [18] CMS Collaboration, “Search for supersymmetry in pp collisions at $\sqrt{s} = 13$ TeV with 137 fb^{-1} in final states with a single lepton using the sum of masses of large-radius jets”, *Phys. Rev. D* **101** (2020) 052010, doi:10.1103/PhysRevD.101.052010, arXiv:1911.07558.
- [19] CMS Collaboration, “Search for supersymmetry in events with one lepton and multiple jets exploiting the angular correlation between the lepton and the missing transverse momentum in proton-proton collisions at $\sqrt{s} = 13$ TeV”, *Phys. Lett. B* **780** (2018) 384, doi:10.1016/j.physletb.2018.03.028, arXiv:1709.09814.
- [20] CMS Collaboration, “Search for supersymmetry in events with one lepton and multiple jets in proton-proton collisions at $\sqrt{s} = 13$ TeV”, *Phys. Rev. D* **95** (2017) 012011, doi:10.1103/PhysRevD.95.012011, arXiv:1609.09386.
- [21] CMS Collaboration, “Search for supersymmetry in pp collisions at $\sqrt{s} = 13$ TeV in the single-lepton final state using the sum of masses of large-radius jets”, *JHEP* **08** (2016) 122, doi:10.1007/JHEP08(2016)122, arXiv:1605.04608.

- [22] CMS Collaboration, “Inclusive search for supersymmetry in pp collisions at $\sqrt{s} = 13$ TeV using razor variables and boosted object identification in zero and one lepton final states”, *JHEP* **03** (2019) 031, doi:10.1007/JHEP03(2019)031, arXiv:1812.06302.
- [23] CMS Collaboration, “Search for supersymmetry in pp collisions at $\sqrt{s} = 13$ TeV in the single-lepton final state using the sum of masses of large-radius jets”, *Phys. Rev. Lett.* **119** (2017) 151802, doi:10.1103/PhysRevLett.119.151802, arXiv:1705.04673.
- [24] ATLAS Collaboration, “Search for squarks and gluinos in final states with jets and missing transverse momentum using 139 fb^{-1} of $\sqrt{s} = 13$ TeV pp collision data with the ATLAS detector”, *JHEP* **02** (2021) 143, doi:10.1007/JHEP02(2021)143, arXiv:2010.14293.
- [25] ATLAS Collaboration, “Search for squarks and gluinos in final states with jets and missing transverse momentum using 36 fb^{-1} of $\sqrt{s} = 13$ TeV pp collision data with the ATLAS detector”, *Phys. Rev. D* **97** (2018) 112001, doi:10.1103/PhysRevD.97.112001, arXiv:1712.02332.
- [26] ATLAS Collaboration, “Summary of the searches for squarks and gluinos using $\sqrt{s} = 8$ TeV pp collisions with the ATLAS experiment at the LHC”, *JHEP* **10** (2015) 054, doi:10.1007/JHEP10(2015)054, arXiv:1507.05525.
- [27] ATLAS Collaboration, “Search for new phenomena in final states with large jet multiplicities and missing transverse momentum using $\sqrt{s} = 13$ TeV proton-proton collisions recorded by ATLAS in Run 2 of the LHC”, *JHEP* **10** (2020) 062, doi:10.1007/JHEP10(2020)062, arXiv:2008.06032.
- [28] CMS Collaboration, “Search for physics beyond the standard model in events with two leptons of same sign, missing transverse momentum, and jets in proton-proton collisions at $\sqrt{s} = 13$ TeV”, *Eur. Phys. J. C* **77** (2017) 578, doi:10.1140/epjc/s10052-017-5079-z, arXiv:1704.07323.
- [29] CMS Collaboration, “Search for new physics in events with same-sign dileptons and jets in pp collisions at $\sqrt{s} = 8$ TeV”, *JHEP* **01** (2014) 163, doi:10.1007/JHEP01(2014)163, arXiv:1311.6736. [Erratum: doi:10.1007/JHEP01(2015)014].
- [30] CMS Collaboration, “Search for supersymmetry in the multijet and missing transverse momentum final state in pp collisions at 13 TeV”, *Phys. Lett. B* **758** (2016) 152, doi:10.1016/j.physletb.2016.05.002, arXiv:1602.06581.
- [31] CMS Collaboration, “Search for supersymmetry in multijet events with missing transverse momentum in proton-proton collisions at 13 TeV”, *Phys. Rev. D* **96** (2017) 032003, doi:10.1103/PhysRevD.96.032003, arXiv:1704.07781.
- [32] CMS Collaboration, “Searches for physics beyond the standard model with the m_{T2} variable in hadronic final states with and without disappearing tracks in proton-proton collisions at $\sqrt{s} = 13$ TeV”, *Eur. Phys. J. C* **80** (2020) 3, doi:10.1140/epjc/s10052-019-7493-x, arXiv:1909.03460.
- [33] CMS Collaboration, “Search for supersymmetry in proton-proton collisions at 13 TeV in final states with jets and missing transverse momentum”, *JHEP* **10** (2019) 244, doi:10.1007/JHEP10(2019)244, arXiv:1908.04722.

- [34] CMS Collaboration, “Search for supersymmetry in proton-proton collisions at 13 TeV using identified top quarks”, *Phys. Rev. D* **97** (2018) 012007, doi:10.1103/PhysRevD.97.012007, arXiv:1710.11188.
- [35] CMS Collaboration, “Search for new phenomena with the m_{T2} variable in the all-hadronic final state produced in proton-proton collisions at $\sqrt{s} = 13$ TeV”, *Eur. Phys. J. C* **77** (2017) 710, doi:10.1140/epjc/s10052-017-5267-x, arXiv:1705.04650.
- [36] HEPData record for this analysis, 2022. doi:10.17182/hepdata.135454.
- [37] CMS Collaboration, “Electron and photon reconstruction and identification with the CMS experiment at the CERN LHC”, *JINST* **16** (2021) P05014, doi:10.1088/1748-0221/16/05/P05014, arXiv:2012.06888.
- [38] CMS Collaboration, “Performance of the CMS muon detector and muon reconstruction with proton-proton collisions at $\sqrt{s} = 13$ TeV”, *JINST* **13** (2018) P06015, doi:10.1088/1748-0221/13/06/P06015, arXiv:1804.04528.
- [39] CMS Collaboration, “Description and performance of track and primary-vertex reconstruction with the CMS tracker”, *JINST* **9** (2014) P10009, doi:10.1088/1748-0221/9/10/P10009, arXiv:1405.6569.
- [40] CMS Collaboration, “Performance of the CMS Level-1 trigger in proton-proton collisions at $\sqrt{s} = 13$ TeV”, *JINST* **15** (2020) P10017, doi:10.1088/1748-0221/15/10/P10017, arXiv:2006.10165.
- [41] CMS Collaboration, “The CMS trigger system”, *JINST* **12** (2017) P01020, doi:10.1088/1748-0221/12/01/P01020, arXiv:1609.02366.
- [42] CMS Collaboration, “The CMS experiment at the CERN LHC”, *JINST* **3** (2008) S08004, doi:10.1088/1748-0221/3/08/S08004.
- [43] J. Alwall et al., “The automated computation of tree-level and next-to-leading order differential cross sections, and their matching to parton shower simulations”, *JHEP* **07** (2014) 079, doi:10.1007/JHEP07(2014)079, arXiv:1405.0301.
- [44] R. Frederix and S. Frixione, “Merging meets matching in MC@NLO”, *JHEP* **12** (2012) 061, doi:10.1007/JHEP12(2012)061, arXiv:1209.6215.
- [45] P. Nason, “A new method for combining NLO QCD with shower Monte Carlo algorithms”, *JHEP* **11** (2004) 040, doi:10.1088/1126-6708/2004/11/040, arXiv:hep-ph/0409146.
- [46] S. Frixione, P. Nason, and C. Oleari, “Matching NLO QCD computations with parton shower simulations: the POWHEG method”, *JHEP* **11** (2007) 070, doi:10.1088/1126-6708/2007/11/070, arXiv:0709.2092.
- [47] S. Alioli, P. Nason, C. Oleari, and E. Re, “A general framework for implementing NLO calculations in shower Monte Carlo programs: the POWHEG BOX”, *JHEP* **06** (2010) 043, doi:10.1007/JHEP06(2010)043, arXiv:1002.2581.
- [48] S. Alioli, P. Nason, C. Oleari, and E. Re, “NLO single-top production matched with shower in POWHEG: s - and t -channel contributions”, *JHEP* **09** (2009) 111, doi:10.1088/1126-6708/2009/09/111, arXiv:0907.4076. [Erratum: doi:10.1007/JHEP02(2010)011].

- [49] E. Re, “Single-top Wt -channel production matched with parton showers using the POWHEG method”, *Eur. Phys. J. C* **71** (2011) 1547, doi:10.1140/epjc/s10052-011-1547-z, arXiv:1009.2450.
- [50] T. Melia, P. Nason, R. Rötsch, and G. Zanderighi, “ W^+W^- , WZ and ZZ production in the POWHEG BOX”, *JHEP* **11** (2011) 078, doi:10.1007/JHEP11(2011)078, arXiv:1107.5051.
- [51] P. Nason and G. Zanderighi, “ W^+W^- , WZ and ZZ production in the POWHEG-BOX-V2”, *Eur. Phys. J. C* **74** (2014) 2702, doi:10.1140/epjc/s10052-013-2702-5, arXiv:1311.1365.
- [52] H. B. Hartanto, B. Jäger, L. Reina, and D. Wackerroth, “Higgs boson production in association with top quarks in the POWHEG BOX”, *Phys. Rev. D* **91** (2015) 094003, doi:10.1103/PhysRevD.91.094003, arXiv:1501.04498.
- [53] T. Sjöstrand et al., “An introduction to PYTHIA 8.2”, *Comput. Phys. Commun.* **191** (2015) 159, doi:10.1016/j.cpc.2015.01.024, arXiv:1410.3012.
- [54] S. Quackenbush, R. Gavin, Y. Li, and F. Petriello, “ W physics at the LHC with FEWZ 2.1”, *Comput. Phys. Commun.* **184** (2013) 209, doi:10.1016/j.cpc.2012.09.005, arXiv:1201.5896.
- [55] R. Gavin, Y. Li, F. Petriello, and S. Quackenbush, “FEWZ 2.0: A code for hadronic Z production at next-to-next-to-leading order”, *Comput. Phys. Commun.* **182** (2011) 2388, doi:10.1016/j.cpc.2011.06.008, arXiv:1011.3540.
- [56] Y. Li and F. Petriello, “Combining QCD and electroweak corrections to dilepton production in the framework of the FEWZ simulation code”, *Phys. Rev. D* **86** (2012) 094034, doi:10.1103/PhysRevD.86.094034, arXiv:1208.5967.
- [57] T. Gehrmann et al., “ W^+W^- production at hadron colliders in next to next to leading order QCD”, *Phys. Rev. Lett.* **113** (2014) 212001, doi:10.1103/PhysRevLett.113.212001, arXiv:1408.5243.
- [58] J. M. Campbell, R. K. Ellis, and C. Williams, “Vector boson pair production at the LHC”, *JHEP* **07** (2011) 018, doi:10.1007/JHEP07(2011)018, arXiv:1105.0020.
- [59] M. Beneke, P. Falgari, S. Klein, and C. Schwinn, “Hadronic top-quark pair production with NNLL threshold resummation”, *Nucl. Phys. B* **855** (2012) 695, doi:10.1016/j.nuclphysb.2011.10.021, arXiv:1109.1536.
- [60] M. Cacciari et al., “Top-pair production at hadron colliders with next-to-next-to-leading logarithmic soft-gluon resummation”, *Phys. Lett. B* **710** (2012) 612, doi:10.1016/j.physletb.2012.03.013, arXiv:1111.5869.
- [61] P. Bärnreuther, M. Czakon, and A. Mitov, “Percent-level-precision physics at the Tevatron: next-to-next-to-leading order QCD corrections to $q\bar{q} \rightarrow t\bar{t} + X$ ”, *Phys. Rev. Lett.* **109** (2012) 132001, doi:10.1103/PhysRevLett.109.132001, arXiv:1204.5201.
- [62] M. Czakon and A. Mitov, “NNLO corrections to top-pair production at hadron colliders: the all-fermionic scattering channels”, *JHEP* **12** (2012) 054, doi:10.1007/JHEP12(2012)054, arXiv:1207.0236.

- [63] M. Czakon and A. Mitov, “NNLO corrections to top pair production at hadron colliders: the quark-gluon reaction”, *JHEP* **01** (2013) 080, doi:10.1007/JHEP01(2013)080, arXiv:1210.6832.
- [64] M. Czakon, P. Fiedler, and A. Mitov, “Total top-quark pair-production cross section at hadron colliders through $O(\alpha_S^4)$ ”, *Phys. Rev. Lett.* **110** (2013) 252004, doi:10.1103/PhysRevLett.110.252004, arXiv:1303.6254.
- [65] M. Czakon and A. Mitov, “TOP++: A program for the calculation of the top-pair cross-section at hadron colliders”, *Comput. Phys. Commun.* **185** (2014) 2930, doi:10.1016/j.cpc.2014.06.021, arXiv:1112.5675.
- [66] W. Beenakker et al., “NNLL-fast: predictions for coloured supersymmetric particle production at the LHC with threshold and Coulomb resummation”, *JHEP* **12** (2016) 133, doi:10.1007/JHEP12(2016)133, arXiv:1607.07741.
- [67] W. Beenakker, R. Höpker, M. Spira, and P. M. Zerwas, “Squark and gluino production at hadron colliders”, *Nucl. Phys. B* **492** (1997) 51, doi:10.1016/S0550-3213(97)80027-2, arXiv:hep-ph/9610490.
- [68] A. Kulesza and L. Motyka, “Threshold resummation for squark-antisquark and gluino-pair production at the LHC”, *Phys. Rev. Lett.* **102** (2009) 111802, doi:10.1103/PhysRevLett.102.111802, arXiv:0807.2405.
- [69] A. Kulesza and L. Motyka, “Soft gluon resummation for the production of gluino-gluino and squark-antisquark pairs at the LHC”, *Phys. Rev. D* **80** (2009) 095004, doi:10.1103/PhysRevD.80.095004, arXiv:0905.4749.
- [70] W. Beenakker et al., “Soft-gluon resummation for squark and gluino hadroproduction”, *JHEP* **12** (2009) 041, doi:10.1088/1126-6708/2009/12/041, arXiv:0909.4418.
- [71] W. Beenakker et al., “NNLL resummation for squark-antisquark pair production at the LHC”, *JHEP* **01** (2012) 076, doi:10.1007/JHEP01(2012)076, arXiv:1110.2446.
- [72] W. Beenakker et al., “Towards NNLL resummation: hard matching coefficients for squark and gluino hadroproduction”, *JHEP* **10** (2013) 120, doi:10.1007/JHEP10(2013)120, arXiv:1304.6354.
- [73] W. Beenakker et al., “NNLL resummation for squark and gluino production at the LHC”, *JHEP* **12** (2014) 023, doi:10.1007/JHEP12(2014)023, arXiv:1404.3134.
- [74] W. Beenakker et al., “Stop production at hadron colliders”, *Nucl. Phys. B* **515** (1998) 3, doi:10.1016/S0550-3213(98)00014-5, arXiv:hep-ph/9710451.
- [75] W. Beenakker et al., “Supersymmetric top and bottom squark production at hadron colliders”, *JHEP* **08** (2010) 098, doi:10.1007/JHEP08(2010)098, arXiv:1006.4771.
- [76] W. Beenakker et al., “NNLL resummation for stop pair-production at the LHC”, *JHEP* **05** (2016) 153, doi:10.1007/JHEP05(2016)153, arXiv:1601.02954.
- [77] M. L. Mangano, M. Moretti, F. Piccinini, and M. Treccani, “Matching matrix elements and shower evolution for top-pair production in hadronic collisions”, *JHEP* **01** (2007) 013, doi:10.1088/1126-6708/2007/01/013, arXiv:hep-ph/0611129.

- [78] CMS Collaboration, “Event generator tunes obtained from underlying event and multiparton scattering measurement”, *Eur. Phys. J. C* **76** (2016) 155, doi:10.1140/epjc/s10052-016-3988-x, arXiv:1512.00815.
- [79] CMS Collaboration, “Extraction and validation of a new set of CMS PYTHIA 8 tunes from underlying-event measurements”, *Eur. Phys. J. C* **80** (2020) 4, doi:10.1140/epjc/s10052-019-7499-4, arXiv:1903.12179.
- [80] NNPDF Collaboration, “Parton distributions for the LHC Run II”, *JHEP* **04** (2015) 040, doi:10.1007/JHEP04(2015)040, arXiv:1410.8849.
- [81] NNPDF Collaboration, “Parton distributions from high-precision collider data”, *Eur. Phys. J. C* **77** (2017) 663, doi:10.1140/epjc/s10052-017-5199-5, arXiv:1706.00428.
- [82] GEANT4 Collaboration, “GEANT4—a simulation toolkit”, *Nucl. Instrum. Meth. A* **506** (2003) 250, doi:10.1016/S0168-9002(03)01368-8.
- [83] CMS Collaboration, S. Abdullin et al., “The fast simulation of the CMS detector at LHC”, in *Proc. 18th Int. Conf. on Computing in High Energy and Nuclear Phys. (CHEP 2010): Taipei, Taiwan, October 18–22, 2010*. 2011. [J. Phys. Conf. Ser. 331 (2011) 032049]. doi:10.1088/1742-6596/331/3/032049.
- [84] A. Giammanco, “The fast simulation of the CMS experiment”, in *Proc. 20th Int. Conf. on Computing in High Energy and Nuclear Phys. (CHEP 2013): Amsterdam, The Netherlands, October 14–18, 2013*. 2014. [J. Phys. Conf. Ser. 513 (2014) 022012]. doi:10.1088/1742-6596/513/2/022012.
- [85] CMS Collaboration, “Particle-flow reconstruction and global event description with the CMS detector”, *JINST* **12** (2017) P10003, doi:10.1088/1748-0221/12/10/P10003, arXiv:1706.04965.
- [86] CMS Collaboration, “Technical proposal for the Phase-II upgrade of the Compact Muon Solenoid”, CMS Technical Proposal CERN-LHCC-2015-010, CMS-TDR-15-02, 2015.
- [87] K. Rehermann and B. Tweedie, “Efficient identification of boosted semileptonic top quarks at the LHC”, *JHEP* **03** (2011) 059, doi:10.1007/JHEP03(2011)059, arXiv:1007.2221.
- [88] M. Cacciari, G. P. Salam, and G. Soyez, “The anti- k_T jet clustering algorithm”, *JHEP* **04** (2008) 063, doi:10.1088/1126-6708/2008/04/063, arXiv:0802.1189.
- [89] M. Cacciari, G. P. Salam, and G. Soyez, “FASTJET user manual”, *Eur. Phys. J. C* **72** (2012) 1896, doi:10.1140/epjc/s10052-012-1896-2, arXiv:1111.6097.
- [90] CMS Collaboration, “Pileup mitigation at CMS in 13 TeV data”, *JINST* **15** (2020) P09018, doi:10.1088/1748-0221/15/09/P09018, arXiv:2003.00503.
- [91] D. Bertolini, P. Harris, M. Low, and N. Tran, “Pileup per particle identification”, *JHEP* **10** (2014) 059, doi:10.1007/JHEP10(2014)059, arXiv:1407.6013.
- [92] CMS Collaboration, “Jet energy scale and resolution in the CMS experiment in pp collisions at 8 TeV”, *JINST* **12** (2017) P02014, doi:10.1088/1748-0221/12/02/P02014, arXiv:1607.03663.

- [93] CMS Collaboration, “Identification of heavy-flavour jets with the CMS detector in pp collisions at 13 TeV”, *JINST* **13** (2018) P05011, doi:10.1088/1748-0221/13/05/P05011, arXiv:1712.07158.
- [94] CMS Collaboration, “Identification of heavy, energetic, hadronically decaying particles using machine-learning techniques”, *JINST* **15** (2020) P06005, doi:10.1088/1748-0221/15/06/P06005, arXiv:2004.08262.
- [95] CMS Collaboration, “Search for direct production of supersymmetric partners of the top quark in the all-jets final state in proton-proton collisions at $\sqrt{s} = 13$ TeV”, *JHEP* **10** (2017) 005, doi:10.1007/JHEP10(2017)005, arXiv:1707.03316.
- [96] CMS Collaboration, “Performance of missing transverse momentum reconstruction in proton-proton collisions at $\sqrt{s} = 13$ TeV using the CMS detector”, *JINST* **14** (2019) P07004, doi:10.1088/1748-0221/14/07/P07004, arXiv:1903.06078.
- [97] C. G. Lester and D. J. Summers, “Measuring masses of semi-invisibly decaying particle pairs produced at hadron colliders”, *Phys. Lett. B* **463** (1999) 99, doi:10.1016/S0370-2693(99)00945-4, arXiv:hep-ph/9906349.
- [98] CMS Collaboration, “Measurement of the polarization of W bosons with large transverse momenta in W+jets events at the LHC”, *Phys. Rev. Lett.* **107** (2011) 021802, doi:10.1103/PhysRevLett.107.021802, arXiv:1104.3829.
- [99] CMS Collaboration, “Search for supersymmetry in pp collisions at $\sqrt{s} = 7$ TeV in events with a single lepton, jets, and missing transverse momentum”, *Eur. Phys. J. C* **73** (2013) 2404, doi:10.1140/epjc/s10052-013-2404-z, arXiv:1212.6428.
- [100] CMS Collaboration, “Measurement of the inelastic proton-proton cross section at $\sqrt{s} = 13$ TeV”, *JHEP* **07** (2018) 161, doi:10.1007/JHEP07(2018)161, arXiv:1802.02613.
- [101] CMS Collaboration, “Precision luminosity measurement in proton-proton collisions at $\sqrt{s} = 13$ TeV in 2015 and 2016 at CMS”, *Eur. Phys. J. C* **81** (2021) 800, doi:10.1140/epjc/s10052-021-09538-2, arXiv:2104.01927.
- [102] CMS Collaboration, “CMS luminosity measurement for the 2017 data-taking period at $\sqrt{s} = 13$ TeV”, CMS Physics Analysis Summary CMS-PAS-LUM-17-004, 2018.
- [103] CMS Collaboration, “CMS luminosity measurement for the 2018 data-taking period at $\sqrt{s} = 13$ TeV”, CMS Physics Analysis Summary CMS-PAS-LUM-18-002, 2019.
- [104] Z. Bern et al., “Left-handed W bosons at the LHC”, *Phys. Rev. D* **84** (2011) 034008, doi:10.1103/PhysRevD.84.034008, arXiv:1103.5445.
- [105] CMS Collaboration, “Angular coefficients of Z bosons produced in pp collisions at $\sqrt{s} = 8$ TeV and decaying to $\mu^+\mu^-$ as a function of transverse momentum and rapidity”, *Phys. Lett. B* **750** (2015) 154, doi:10.1016/j.physletb.2015.08.061, arXiv:1504.03512.
- [106] ATLAS Collaboration, “Measurement of the polarisation of W bosons produced with large transverse momentum in pp collisions at $\sqrt{s} = 7$ TeV with the ATLAS experiment”, *Eur. Phys. J. C* **72** (2012) 2001, doi:10.1140/epjc/s10052-012-2001-6, arXiv:1203.2165.

- [107] ATLAS Collaboration, “Measurement of the W boson polarization in top quark decays with the ATLAS detector”, *JHEP* **06** (2012) 088, doi:10.1007/JHEP06(2012)088, arXiv:1205.2484.
- [108] ATLAS Collaboration, “Measurement of the inelastic proton-proton cross section at $\sqrt{s} = 13$ TeV with the ATLAS detector at the LHC”, *Phys. Rev. Lett.* **117** (2016) 182002, doi:10.1103/PhysRevLett.117.182002, arXiv:1606.02625.
- [109] CMS Collaboration, “Measurement of top quark polarisation in t -channel single top quark production”, *JHEP* **04** (2016) 073, doi:10.1007/JHEP04(2016)073, arXiv:1511.02138.
- [110] ATLAS Collaboration, “Measurement of the W boson polarisation in $t\bar{t}$ events from pp collisions at $\sqrt{s} = 8$ TeV in the lepton+jets channel with ATLAS”, *Eur. Phys. J. C* **77** (2017) 264, doi:10.1140/epjc/s10052-017-4819-4, arXiv:1612.02577. [Erratum: doi:10.1140/epjc/s10052-018-6520-7].
- [111] CMS Collaboration, “Measurement of the $t\bar{t}$ production cross section using events with one lepton and at least one jet in pp collisions at $\sqrt{s} = 13$ TeV”, *JHEP* **09** (2017) 051, doi:10.1007/JHEP09(2017)051, arXiv:1701.06228.
- [112] T. Junk, “Confidence level computation for combining searches with small statistics”, *Nucl. Instrum. Meth. A* **434** (1999) 435, doi:10.1016/S0168-9002(99)00498-2, arXiv:hep-ex/9902006.
- [113] A. Read, “Presentation of search results: the CL_s technique”, *J. Phys. G* **28** (2002) 2693, doi:10.1088/0954-3899/28/10/313.
- [114] G. Cowan, K. Cranmer, E. Gross, and O. Vitells, “Asymptotic formulae for likelihood-based tests of new physics”, *Eur. Phys. J. C* **71** (2011) 1554, doi:10.1140/epjc/s10052-011-1554-0, arXiv:1007.1727. [Erratum: doi:10.1140/epjc/s10052-013-2501-z].